Two volcanic tsunami events caused by trapdoor faulting at a submerged caldera near Curtis and Cheeseman Islands in the Kermadec Arc

Osamu Sandanbata[1], Shingo Watada[2], Kenji Satake[2], Hiroo Kanamori[3], and Luis Rivera[4]

[1]National Research Institute for Earth Science and Disaster Resilience
[2]University of Tokyo
[3]Seismological Laboratory, California Institute of Technology
[4]Université de Strasbourg

December 28, 2022

Abstract

Two unusual submarine earthquakes (Mw 5.8) occurred near volcanic islands, called Curtis and Cheeseman, in the Kermadec Arc in 2009 and 2017. Following both earthquakes, similar tsunamis with wave heights of about a meter, that are disproportionate to their moderate seismic magnitudes, were observed by coastal tide gauges. We investigate the source mechanism for both earthquakes by analyzing tsunami and seismic data of the 2017 event. Preliminary analysis of tsunami data indicates that the earthquake uplifted a submerged caldera around the islands. Source modeling using tsunami and seismic data reveals that a trapdoor faulting, involving ring-faulting and deformation of an underlying magma reservoir, occurred due to magma overpressure in the reservoir, possibly in association with caldera resurgence. The relationship between the maximum fault slip and the seismic magnitude for trapdoor faulting events found at global calderas is different from that for regular earthquakes, reflecting the peculiarity of the volcanic earthquakes.

Two volcanic tsunami events caused by trapdoor faulting at a submerged caldera near Curtis and Cheeseman Islands in the Kermadec Arc

Osamu Sandanbata[1,2†], Shingo Watada[1], Kenji Satake[1], Hiroo Kanamori[3], and Luis Rivera[4]

[1] Earthquake Research Institute, the University of Tokyo, Tokyo, Japan.

[2] National Research Institute for Earth Science and Disaster Resilience, Ibaraki, Japan.

[3] Seismological Laboratory, California Institute of Technology, Pasadena, CA, USA.

[4] Université de Strasbourg, CNRS, ITES UMR 7063, Strasbourg F-67084, France.

Corresponding author: Osamu Sandanbata (osm3@bosai.go.jp)

†*Now at* National Research Institute for Earth Science and Disaster Resilience, Ibaraki, Japan.

Key Points:

- Unusual tsunamis were caused by two M_w 5.8 volcanic earthquakes in 2009 and 2017 near Curtis and Cheeseman Islands in the Kermadec Arc.
- By analyzing tsunami and seismic data of the 2017 event, we suggest that the trapdoor faulting occurred at a submerged resurgent caldera.
- Trapdoor faulting found at global calderas had abnormally large fault slips, implying their atypical earthquake physics.

Abstract

Two submarine earthquakes (M_w 5.8) occurred near volcanic islands, Curtis and Cheeseman, in the Kermadec Arc in 2009 and 2017. Following both earthquakes, similar tsunamis with wave heights of about a meter, larger than expected from their moderate seismic magnitudes, were observed by coastal tide gauges. We investigate the source mechanism for both earthquakes by analyzing tsunami and seismic data of the 2017 event. Tsunami waveform analysis indicates that the earthquake uplifted a submerged caldera around the islands. Combined analysis of tsunami and seismic data suggests that *trapdoor faulting*, involving intra-caldera fault slip and magma reservoir deformation, occurred due to magma overpressure in the reservoir, possibly in association with caldera resurgence. The relationship between the fault slip and seismic magnitude for trapdoor faulting at global calderas is different from that for regular earthquakes, reflecting the peculiar earthquake physics at calderas.

Plain Language Summary

Most tsunamis are generated by large earthquakes with seismic magnitudes $M > \sim 7$, but two moderate-sized earthquakes with only M 5.8 near volcanic islands, north of New Zealand, generated unusual tsunamis with a maximum wave height of about a meter. In this study, we examine the unusual source mechanism of the volcanic earthquakes that caused unexpected tsunamis. By analyzing the records of tsunamis and seismic waves from the earthquakes, we suggest that the inside of a curved fault system beneath a submerged volcano with a caldera structure suddenly moved upward, together with a large intra-caldera fault slip and a volume increase of a shallow magma reservoir. Overpressure created by magma accumulation beneath the submarine caldera recurrently induces meter-scale tsunamis without significant ground motions, calling for attention to tsunami hazards from submarine calderas.

1 Introduction

On 17 February 2009 and 8 December 2017 (UTC), peculiar tsunamis were recorded at coastal tide gauges for tsunami monitoring in New Zealand, after shallow earthquakes with moment magnitudes M_w 5.8. Both earthquakes occurred near Curtis and Cheeseman Islands, volcanic islands in the Kermadec Arc (Figure 1a; Table S1); we hereafter call them *Curtis earthquakes*. The maximum tsunami wave heights from the 2009 and 2017 earthquakes were about 50 cm (LOTT) and 80 cm (RFRT), respectively (Figure 1b), much larger than expected for their seismic magnitudes (Abe, 1981). The tsunami waveforms from these earthquakes were similar at three stations, LOTT, NCPT, and TAUT, and their moment tensors are similarly dominated by the compensated-linear-vector-dipole (CLVD) component with a nearly vertical tension-axis, which are types of *vertical-T CLVD earthquake* often observed in active volcanic contexts (Sandanbata, Kanamori, et al., 2021; Shuler, Ekström, et al., 2013; Shuler, Nettles, et al., 2013). These indicate that similar volcanic phenomena causing tsunamis repeated near the islands.

The mechanism of such tsunamigenic vertical-T CLVD earthquakes has been controversial. For the Curtis earthquakes, Gusman et al. (2020) analyzed tsunami data at tide gauges and broad-band (20–500 s) seismic data at Global Seismograph Network and proposed a mechanism involving two sources at different depths. They suggested that a hydrofracturing source at a depth of ~1.5 km in the crust generated tsunamis without significant seismic radiations, and a deeper source at ~10 km related to fluid flow radiated seismic waves. Similar

tsunamigenic vertical-T CLVD earthquakes were observed at Sumisu caldera, south of Japan, for which various mechanisms were proposed: hydrofracturing of magma-water interaction (Kanamori et al., 1993; Satake & Kanamori, 1991), ring-faulting (Ekström, 1994), shallow tensile crack (Fukao et al., 2018). Recently, Sandanbata et al. (2022) showed that trapdoor faulting explains both tsunami and long-period seismic waveforms from an event at Sumisu caldera.

We investigate the source mechanism of the Curtis earthquakes using tsunami and seismic data from the 2017 earthquake by taking a similar approach as done by Sandanbata et al. (2022). We first use tsunami data to estimate the vertical sea-surface displacement due to the earthquake. We then explore a unified source model explaining both tsunami and long-period seismic data. Finally, we propose a source mechanism and discuss submarine volcanism and its atypical earthquake scaling relationship.

2 Geological background

Curtis and Cheeseman Islands are the emergent portions of a submarine dacitic volcano containing a crater with fumaroles activity (Doyle et al., 1979; Smith et al., 1988; Global Volcanism Program, 2013). Doyle et al. (1979) reported a remarkable uplift of 18 m during 200 years on/around the islands, implying active magma supply. Beneath the islands, a cone structure is surrounded by a circular bathymetric depression with a maximum water depth of ~400 m, indicating a submerged caldera with a size of 7 km × 6 km (Figure 2a), as mentioned in Global Volcanism Program (2013); we hereafter call it *Curtis caldera*.

3 Data

3.1 Tsunami data

We use four tsunami waveform data from the 2017 earthquake, recorded at four coastal tide gauges, RBCT, RFRT, LOTT, and GBIT, with a sampling rate of one sample/minute (Figure 1b). We extract the tsunami signals from the raw record by removing tidal trends approximated as low-order polynomial functions. The signals have dominant periods from 200 s to 500 s. We do not use data from NCPT and TAUT, because of poor signal-to-noise ratios.

3.2 Long-period seismic data

We use long-period seismic waveform data from the 2017 earthquake, recorded on LH or BH channels at seismic stations (network codes: IU, NZ, AU, and G). We select 33 good-quality records after data screening, remove the instrument response from the seismograms to obtain displacement records, and apply a causal fourth-order Butterworth band-pass filter with corner frequencies at 0.005 and 0.0125 Hz (period: 80–200 s); these procedures are performed with the W-phase package (Duputel et al., 2012; Hayes et al., 2009; Kanamori & Rivera, 2008).

4 Source modeling of the 2017 earthquake

4.1 Vertical sea-surface displacement model

We start our modeling by estimating the vertical sea-surface displacement due to the 2017 earthquake with the tsunami data (see Text S1, for details). We first simulate dispersive

tsunami waveforms at the tide gauges with the JAGURS code (Baba et al., 2015). We delayed the waveforms at two distant stations, LOTT and GBIT, to incorporate the effects of seawater compressibility and Earth's elasticity (Ho et al., 2017; Sandanbata, Watada, et al., 2021; Watada et al., 2014). We then perform a tsunami waveform inversion to reconstruct the vertical sea-surface displacement.

The obtained model (Figure 2b) involves a large uplift of ~1.3 m localized on the western caldera, a peripheral subsidence of ~1.3 m to the south of the uplift, and another meter-scale uplift to the southeast. This model explains the tsunami data well (Figure 2c). To examine the model robustness, we estimate a sea-surface *uplift* model without subsidence by imposing the non-negative condition on the inversion. In the obtained uplift model (Figure 2d), a localized uplift is estimated similarly over the western caldera but with a larger amplitude of ~2.4 m. In this case, the uplift to the southeast seen in Figure 2b disappears. Despite the model differences, the tsunami waveform fit of this uplift model is comparable to that of the model with both uplift and subsidence (compare Figures 2c and 2e). These results suggest that the tsunami was excited mainly by an uplift localized in the western caldera, as supported by our resolution tests (see Text S1).

Given the inferred co-seismic deformation localized on one side of the caldera, *trapdoor faulting* (Figure 3a) would be a good candidate for the source mechanism. This mechanism, driven by magma pressure in a reservoir, was first proposed for seismic events at a subaerial caldera of Sierra Negra volcano, Galapagos (e.g., Amelung et al., 2000; Zheng et al., 2022), and recently found at Sumisu caldera in oceans (Sandanbata et al., 2022). These studies showed that trapdoor faulting can be considered as a combination of a sudden slip of a part of an intra-caldera fault and an asymmetric deformation of a crack-like reservoir. This mechanism generates a large asymmetric caldera uplift with a vertical-T CLVD earthquake, as observed from the Curtis earthquake.

4.2 Dislocation model of the fault-crack composite source

Considering the mechanism, we explore an earthquake source model by using both the tsunami and long-period seismic data, following the methodology of Sandanbata et al. (2022) (see Text S2, for details). First, we assume a fault-crack composite source system, or an inward-dipping partial ring fault connected to a horizontal crack at a depth of 3 km in the crust (Figures 3b and S1). We fix the partial ring fault on the western side of the caldera (Figure 3b), given the uplift over the western caldera (Figure 2a); the dip angle is varied from 65–85°. Second, by a tsunami waveform inversion, we determine dislocations of the source system, i.e., reverse slips of the ring fault and vertical opening/closure of the horizontal crack, to obtain source models. We assume a reverse slip on an inward-dipping ring fault because this combination can cause a vertical-T CLVD earthquake that accompanies a caldera uplift (see Figure 1 in Sandanbata, Kanamori, et al., 2021). Here, the vertical component of the slip at the fault bottom is assumed to be the same as the opening of the horizontal crack at its contact. Third, we compute long-period (80–200 s) seismograms from the models and compare them with the seismic data for validation.

Consequently, we find source models that explain both datasets. First, the tsunami waveform inversion successfully determines the dislocations of the fault-crack composite source system, as shown by an example model in Figure 3b. The model is expected to uplift the sea surface by ~2 m (Figure 4a), explaining the tsunami data well (Figure 4b). Although we

vary the ring-fault dip angle, all the obtained models yield similarly good waveform fit (Figure S2) with small waveform misfits (tsunami NRMS of 0.60–0.76; Figure 3c), indicating weak constraints on the dip angle.

In contrast, long-period seismic wave amplitudes from the models change significantly depending on the dip angle (Figure S3), resulting in large variations of the misfit of seismic waveforms (seismic RMS of 0.86–2.08 μm; Figure 3c). This is because seismic excitation by a shallow ring-faulting becomes less efficient as the dip is close to vertical (Sandanbata, Kanamori, et al., 2021). Thus, models with dip angles in a narrow range of 75° to 81° yield reasonable seismic waveform fits (seismic RMS <1.0 μm; Figure 3c). Figures 4c–e shows moment tensors and long-period seismograms computed from the model shown in Figure 3b, which has a ring-fault dip angle of 78°; this model explains the seismic waveform data well (Figure 3e), yielding the smallest seismic RMS of 0.86 μm (Figure 3c).

Therefore, we propose the model shown in Figure 3b as a best-fit source model. It presents a reverse slip of 4.4 m at a maximum along the ring fault with a dip angle of 78° and asymmetric opening and closure of the horizontal crack with maximum amounts of 5.4 m and 2.9 m, respectively. The crack increases its inner volume by $+3.5 \times 10^7$ m^3. This model causes a sea-surface uplift localized over the western caldera with a smaller subsidence outside of the fault (Figure 4a). The pattern and amplitude of this sea-surface displacement are different from those estimated in Section 4.1 (Figures 2b and 2d) due to strong constraints from the fault-crack source system, but this model explains the tsunami data well (Figure 4b). Figure S4 shows synthetic tsunami waveforms from the horizontal crack and the ring fault separately, demonstrating that both parts contribute the tsunami generation.

The model's total moment tensor is highly isotropic with M_w 6.24 (Figure 4c; Table S2), composed of the horizontal crack (M_w 6.19) with a strong isotropic component and the ring fault (M_w 5.96) with a large vertical-T CLVD component (Figure 4d). In Figure S5, we show that only limited components of the ring fault, which constitute a vertical-T CLVD moment tensor, mainly contribute to the seismic radiation, and that the horizontal crack contributes little (see Text S3, for details). This explains why vertical-T CLVD moment tensors were obtained by moment tensor analyses assuming no isotropic component, as seen in the GCMT catalog.

5 Discussion

5.1 Trapdoor faulting mechanism

We have shown that our source model (Figure 3b) explains both the tsunami and long-period seismic data from the 2017 Curtis earthquake. The asymmetrical motion of the source system is like those estimated for trapdoor faulting at Sumisu and Sierra Negra calderas (e.g., Sandanbata et al., 2022; Zheng et al., 2022). Following the interpretations of the previous studies, we suggest that trapdoor faulting occurred at Curtis caldera, as follows. Before trapdoor faulting, the caldera gradually inflated due to continuous magma influx into the reservoir, and the magma pressurization increased shear stress on an inward-dipping ring fault. At the time of trapdoor faulting, the western fault suddenly slips in a reverse sense due to the critically increased shear stress created by the magma pressure. The fault slip instantaneously moves up the upper wall of the western crack and expands the crack near the fault. The asymmetrical crack expansion induces magma flow from the eastern to western sides of the

196 crack, which results in the closure of the eastern crack with magma depressurization; the crack
197 closure might be alternatively caused by magma mass outflow due to an eruption, but the two
198 possible cases are indistinguishable from the available dataset.

199 Given the similarities between the Curtis earthquakes in 2009 and 2017, we suggest that
200 the trapdoor faulting recurred at Curtis caldera. The tsunami waveforms from the earthquakes
201 are almost identical at LOTT, NCPT, and TAUT (Figure 1b). To further investigate the
202 earthquake similarity, we perform deviatoric moment tensor analysis using long-period seismic
203 data (Table S3; see Text S6). We neglect two moment-tensor elements, $M_{r\theta}$ and $M_{r\varphi}$, that are
204 indeterminate for such shallow earthquakes to obtain *resolvable moment tensors* $\boldsymbol{M}_{res}$ as
205 proxies for the ring-fault geometry (Sandanbata, Kanamori, et al., 2021) (Figure S6). Similar
206 null-axis directions (NNW-SSE) of $\boldsymbol{M}_{res}$ indicate that ring-fault segments of the two events are
207 oriented similarly, while a more dominant vertical-CLVD component of the 2017 event (larger
208 k_{CLVD}; see the definition in Text S4) implies that a longer ring fault was ruptured by this event
209 than the 2009 event. Recurrence of trapdoor faulting was reported for Sumisu and Sierra Negra
210 calderas, being attributed to continuous magma supply causing fault failures repeatedly (Gregg
211 et al., 2022; Bell, Hernandez, et al., 2021; Sandanbata et al., 2022); this would be the case for
212 Curtis caldera.

213 Due to little information on the sub-caldera structure and our datasets with long-period
214 properties (>~100 s) mostly at far field, our analysis has limited constraints on detailed source
215 geometries. For example, in Text S5, we demonstrate that different fault-crack composite
216 source models with a deeper crack, a longer ring fault, or an additional normal faulting
217 component on the eastern fault, also reproduce the datasets. For constraints on such details,
218 further investigations using near-field data or better structural information would be required.
219 Yet, we emphasize that the trapdoor faulting mechanism is still inferred from these alternative
220 models. We also note that fault-crack composite source models explain the tsunami and
221 seismic datasets better than models of only a ring fault or of only a horizontal crack (see Text
222 S6, for details); the tsunami data are not reproduced well by only a ring fault, while the seismic
223 data cannot be reproduced by only a horizontal crack.

224 Gusman et al. (2020) suggested a different mechanism for these earthquakes to explain
225 tsunami and broadband seismic waveforms. They separately attributed the tsunami generation
226 to a hydrofracturing source at a shallow depth and the vertical-T CLVD seismic radiation to a
227 deeper source. On the other hand, we demonstrated that trapdoor faulting at a shallow depth
228 beneath the caldera reproduces tsunami and long-period seismic waveforms. The two
229 mechanisms seem indistinguishable from the available tsunami data. Given the difficulty in
230 determining source depths of shallow seismic sources (Ekström et al., 2012) and the
231 complexity of shallow seismic sources involving volume changes (Kawakatsu et al., 1996), it
232 would be also challenging to distinguish the two mechanisms from available regional- to far-
233 field seismic data.

234 5.2 Implications for submarine volcanism

235 The trapdoor faulting may have occurred in the *resurgence* process of Curtis caldera.
236 Resurgence is a long-term caldera uplift driven by the gradual pressure increase of magma
237 accumulating in a shallow reservoir and facilitated by reactivations of ring faults, as observed
238 at many calderas like Toba, Long Volley, Valles, and Iwo-Jima (Iō Tō). Although most
239 resurgent calderas accompany earthquakes with only seismic magnitudes $M < \sim 3$ (Acocella et

al., 2015; references therein), M~5 trapdoor faulting events occurred during the resurgence of Sierra Negra caldera (Bell, La Femina, et al., 2021; Gregg et al., 2018, 2022). The significant uplift on/around Curtis Island found by Doyle et al. (1979) may be a result of the resurgence in the past. The cone structure within the caldera (Figure 2a) is possibly a *resurgent dome*, as seen within many resurgent calderas (Acocella, 2019; Acocella et al., 2001) and replicated by numerical/analog experiments (Acocella & Funiciello, 1999; Brothelande et al., 2016). Active fumaroles found on the island (Doyle et al., 1979) are common features for resurgent domes (Cole et al., 2005; Molin et al., 2003).

The relationship between trapdoor faulting and submarine eruptions at Curtis caldera remains unclear. About a month before the 2009 earthquake, ocean acoustic waves from near the caldera were recorded by a seismic network (Global Volcanism Program, 2013). These signals perhaps indicated submarine eruptions, but their origins are yet to be confirmed.

5.3 Earthquake scaling relationship for trapdoor faulting

The earthquake scaling relationship of trapdoor faulting is distinct from those for tectonic earthquakes. Figure 5 shows the seismic magnitude and the maximum fault slip during four trapdoor faulting events at three calderas, for which source models have been proposed: events on 8 December 2017 at Curtis (M_w 5.8 and 4.4 m [this study]), 2 May 2015 at Sumisu (M_w 5.7 and 6.8 m [Sandanbata et al., 2022]), and 16 April 2005 (m_b 4.6 and 2.0 m [Zheng et al., 2022]; m_b is used for this event because M_w was not reported) and 22 October 2005 (M_w 5.4 and 1.8 m [Yun, 2007]) at Sierra Negra. Compared with the empirical scaling relationship by Wells & Coppersmith (1994), trapdoor faulting involves far larger, 10–20 times, fault slip than those by tectonic earthquakes with similar magnitudes. This peculiarity reflects the atypical earthquake physics of trapdoor faulting that occurs in a fault-reservoir interactive system, which makes trapdoor faulting tsunamigenic, combined with other effects of the shallow depth and curved fault structure (Sandanbata et al., 2022). Shuler, Ekström, et al. (2013) reported longer source durations of volcanic vertical-CLVD earthquakes compared to those of similar-sized tectonic earthquakes, which also suggests peculiar earthquake characters in volcanic regions.

6 Conclusions

Both the seismic and tsunami data from two peculiar earthquakes near Curtis and Cheeseman Islands are explained well by the trapdoor faulting mechanism within the submerged caldera. The large tsunamis can be attributed to the significant caldera-floor displacement caused by an asymmetric caldera motion. Caldera volcanism involving the fault-reservoir interaction would make abnormally large fault slips possible, contributing to large tsunamis. A long-term resurgence of Curtis caldera, inferred from bathymetric and geological features, suggests the importance of volcano monitoring for assessing its eruption potential in the future.

Acknowledgments

We thank Editor, Christian Huber, and two anonymous reviewers for their constructive suggestions. We also thank Zhongwen Zhan for the helpful discussion. This study is funded by the JSPS KAKENHI (JP17J02919, JP20J01689, and JP19K04034), by the JST J-RAPID (JPMJJR1805). Osamu Sandanbata's travel to California Institute of Technology was supported by Oversea Internship Program of Earthquake Research Institute, the University of Tokyo.

Data availability

The tide-gauge data are provided from Land Information New Zealand (LINZ; https://www.linz.govt.nz/sea/tides/sea-level-data/sea-level-data-downloads). The topography and bathymetry data are provided from GEBCO Compilation Group through the British Oceanographic Data Centre (Weatherall et al., 2015; https://www.gebco.net/data_and_products/gridded_bathymetry_data/gebco_30_second_grid/), the National Institute of Water and Atmospheric Research in New Zealand (NIWA; https://niwa.co.nz/our-science/oceans/bathymetry), and LINZ (https://data.linz.govt.nz/). The seismic data are available through the Data Management Center of the Incorporated Research Institutions for Seismology (IRIS)'s Wilber 3 system (https://ds.iris.edu/wilber3/) or IRIS Web Services (https://service.iris.edu/), including the seismic networks of IU (GSN; Albuquerque Seismological Laboratory, 1988), AU (ANSN; H., G., & Geoscience Australia, 2021), NZ (New Zealand National Seismograph Network), and G (GEOSCOPE; IPGP & EOST, 1982). The earthquake information is available from the GCMT catalog (Ekström et al., 2012; https://www.globalcmt.org/https://www.globalcmt.org/). The W-phase package (Duputel et al., 2012; Hayes et al., 2009; Kanamori & Rivera, 2008) is available through the website of W Phase source inversion (http://eost.u-strasbg.fr/wphase/index.html). We plotted focal mechanisms representing moment tensors with a MATLAB code developed by James Conder (available from https://www.mathworks.com/matlabcentral/fileexchange/61227-focalmech-fm-centerx-centery-diam-varargin). The best-fit source model presented in this paper is contained in Data Set S1.

References

Abe, K. (1981). Physical size of tsunamigenic earthquakes of the northwestern Pacific. *Physics of the Earth and Planetary Interiors*, *27*(3), 194–205. https://doi.org/10.1016/0031-9201(81)90016-9

Acocella, V. (2019). Bridging the Gap From Caldera Unrest to Resurgence. *Frontiers of Earth Science in China*, *7*, 173. https://doi.org/10.3389/feart.2019.00173

Acocella, V., & Funiciello, R. (1999). The interaction between regional and local tectonics during resurgent doming: the case of the island of Ischia, Italy. *Journal of Volcanology and Geothermal Research*, *88*(1–2), 109–123. https://doi.org/10.1016/s0377-0273(98)00109-7

Acocella, V., Cifelli, F., & Funiciello, R. (2001). The control of overburden thickness on resurgent domes: insights from analogue models. *Journal of Volcanology and Geothermal Research*, *111*(1–4), 137–153. https://doi.org/10.1016/s0377-0273(01)00224-4

Acocella, V., Funiciello, R., Marotta, E., Orsi, G., & de Vita, S. (2004). The role of extensional structures on experimental calderas and resurgence. *Journal of Volcanology and Geothermal Research*, *129*(1), 199–217. https://doi.org/10.1016/S0377-0273(03)00240-3

Acocella, V., Di Lorenzo, R., Newhall, C., & Scandone, R. (2015). An overview of recent (1988 to 2014) caldera unrest: Knowledge and perspectives. *Reviews of Geophysics* , *53*(3), 896–955. https://doi.org/10.1002/2015rg000492

Aki, K., & Richards, P. G. (1980). *Quantitative seismology: theory and methods* (Vol. 842). Freeman San Francisco, CA.

Amelung, F., Jónsson, S., Zebker, H., & Segall, P. (2000). Widespread uplift and 'trapdoor' faulting on Galápagos volcanoes observed with radar interferometry. *Nature*, *407*(6807), 993–996. https://doi.org/10.1038/35039604

Albuquerque Seismological Laboratory (ASL)/USGS. (1988). Global Seismograph Network - IRIS/USGS [Data set]. International Federation of Digital Seismograph Networks. https://doi.org/10.7914/SN/IU

Baba, T., Takahashi, N., Kaneda, Y., Ando, K., Matsuoka, D., & Kato, T. (2015). Parallel Implementation of Dispersive Tsunami Wave Modeling with a Nesting Algorithm for the 2011 Tohoku Tsunami. *Pure and Applied Geophysics*, *172*(12), 3455–3472. https://doi.org/10.1007/s00024-015-1049-2

Bell, A. F., La Femina, P. C., Ruiz, M., Amelung, F., Bagnardi, M., Bean, C. J., et al. (2021). Caldera resurgence during the 2018 eruption of Sierra Negra volcano, Galápagos Islands. *Nature Communications*, *12*(1), 1397. https://doi.org/10.1038/s41467-021-21596-4

Bell, A. F., Hernandez, S., La Femina, P. C., & Ruiz, M. C. (2021). Uplift and seismicity driven by magmatic inflation at Sierra Negra volcano, Galápagos islands. *Journal of Geophysical Research, [Solid Earth]*, *126*(7). https://doi.org/10.1029/2021jb022244

Brothelande, E., Peltier, A., Got, J.-L., Merle, O., Lardy, M., & Garaebiti, E. (2016). Constraints on the source of resurgent doming inferred from analogue and numerical modeling — Implications on the current feeding system of the Yenkahe dome–Yasur volcano complex (Vanuatu). *Journal of Volcanology and Geothermal Research*, *322*, 225–240. https://doi.org/10.1016/j.jvolgeores.2015.11.023

Cole, J. W., Milner, D. M., & Spinks, K. D. (2005). Calderas and caldera structures: a review. *Earth-Science Reviews*, *69*(1), 1–26. https://doi.org/10.1016/j.earscirev.2004.06.004

Dahlen, F. A., & Tromp, J. (1998). *Theoretical Global Seismology*. Princeton University Press. https://doi.org/10.1515/9780691216157

Doyle, A. C., Singleton, R. J., & Yaldwyn, J. C. (1979). Volcanic activity and recent uplift on Curtis and Cheeseman Islands, Kermadec Group, Southwest Pacific. *Journal of the Royal Society of New Zealand*, *9*(1), 123–140. https://doi.org/10.1080/03036758.1979.10418159

Duputel, Z., Rivera, L., Kanamori, H., & Hayes, G. (2012). W phase source inversion for moderate to large earthquakes (1990–2010). *Geophysical Journal International*, *189*(2), 1125–1147. https://doi.org/10.1111/j.1365-246X.2012.05419.x

Dziewonski, A. M., & Anderson, D. L. (1981). Preliminary reference Earth model. *Physics of the Earth and Planetary Interiors*, *25*(4), 297–356. https://doi.org/10.1016/0031-9201(81)90046-7

Ekström, G. (1994). Anomalous earthquakes on volcano ring-fault structures. *Earth and Planetary Science Letters*, *128*(3–4), 707–712. https://doi.org/10.1016/0012-821x(94)90184-8

Ekström, G., Nettles, M., & Dziewoński, A. M. (2012). The global CMT project 2004–2010: Centroid-moment tensors for 13,017 earthquakes. *Physics of the Earth and Planetary Interiors*, *200-201*, 1–9. https://doi.org/10.1016/j.pepi.2012.04.002

Fukao, Y., Sandanbata, O., Sugioka, H., Ito, A., Shiobara, H., Watada, S., & Satake, K. (2018). Mechanism of the 2015 volcanic tsunami earthquake near Torishima, Japan. *Science Advances*, *4*(4), eaao0219. https://doi.org/10.1126/sciadv.aao0219

Global Volcanism Program. (2013). Curtis Island (242010). In E. Venzke (Ed.), *Volcanoes of the World, v. 4.10.2 (24 Aug 2021)*. Smithsonian Institution. Retrieved from https://volcano.si.edu/volcano.cfm?vn=242010

Gregg, P. M., Le Mével, H., Zhan, Y., Dufek, J., Geist, D., & Chadwick, W. W., Jr. (2018). Stress triggering of the 2005 eruption of Sierra Negra volcano, Galápagos. *Geophysical Research Letters*, *45*(24), 13288–13297. https://doi.org/10.1029/2018gl080393

Gregg, P. M., Zhan, Y., Amelung, F., Geist, D., Mothes, P., Koric, S., & Yunjun, Z. (2022). Forecasting mechanical failure and the 26 June 2018 eruption of Sierra Negra Volcano, Galápagos, Ecuador. *Science Advances*, *8*(22), eabm4261. https://doi.org/10.1126/sciadv.abm4261

Gusman, A. R., Kaneko, Y., Power, W., & Burbidge, D. (2020). Source process for two enigmatic repeating vertical-T CLVD tsunami earthquakes in the kermadec ridge. *Geophysical Research Letters*, *47*(16). https://doi.org/10.1029/2020gl087805

Hanks, T. C., & Kanamori, H. (1979). A moment magnitude scale. *Journal of Geophysical Research*, *84*(B5), 2348. https://doi.org/10.1029/jb084ib05p02348

Hayes, G. P., Rivera, L., & Kanamori, H. (2009). Source Inversion of the W-Phase: Real-time Implementation and Extension to Low Magnitudes. *Seismological Research Letters*, *80*(5), 817–822. https://doi.org/10.1785/gssrl.80.5.817

Ho, T.-C., Satake, K., & Watada, S. (2017). Improved phase corrections for transoceanic tsunami data in spatial and temporal source estimation: Application to the 2011 Tohoku earthquake. *Journal of Geophysical Research, [Solid Earth]*, *122*(12), 10155–10175. https://doi.org/10.1002/2017jb015070

H., G., & Geoscience Australia. (2021). Australian National Seismograph Network Data Collection [Data set]. Commonwealth of Australia (Geoscience Australia). https://doi.org/10.26186/144675

Institut de physique du globe de Paris (IPGP), & École et Observatoire des Sciences de la Terre de Strasbourg (EOST). (1982). GEOSCOPE, French Global Network of broad band seismic stations [Data set]. Institut de physique du globe de Paris (IPGP), Université de Paris. https://doi.org/10.18715/GEOSCOPE.G

Jónsson, S. (2009). Stress interaction between magma accumulation and trapdoor faulting on Sierra Negra volcano, Galápagos. *Tectonophysics*, *471*(1), 36–44. https://doi.org/10.1016/j.tecto.2008.08.005

Kajiura, K. (1963). The Leading Wave of a Tsunami. *Bulletin of the Earthquake Research Institute, University of Tokyo*, *41*(3), 535–571. Retrieved from https://ci.nii.ac.jp/naid/120000866529/

Kanamori, H. (1977). The energy release in great earthquakes. *Journal of Geophysical Research*, *82*(20), 2981–2987. https://doi.org/10.1029/jb082i020p02981

Kanamori, H., & Given, J. W. (1981). Use of long-period surface waves for rapid determination of earthquake-source parameters. *Physics of the Earth and Planetary Interiors*, *27*(1), 8–31. https://doi.org/10.1016/0031-9201(81)90083-2

Kanamori, H., & Rivera, L. (2008). Source inversion of Wphase: speeding up seismic tsunami warning. *Geophysical Journal International*, *175*(1), 222–238. https://doi.org/10.1111/j.1365-246X.2008.03887.x

Kanamori, H., Ekström, G., Dziewonski, A., Barker, J. S., & Sipkin, S. A. (1993). Seismic radiation by magma injection: An anomalous seismic event near Tori Shima, Japan. *Journal of Geophysical Research*, *98*(B4), 6511–6522. https://doi.org/10.1029/92jb02867

Kawakatsu, H. (1996). Observability of the isotropic component of a moment tensor. *Geophysical Journal International*, *126*(2), 525–544. https://doi.org/10.1111/j.1365-246X.1996.tb05308.x

Kawakatsu, H., & Yamamoto, M. (2015). 4.15 - Volcano Seismology. In G. Schubert (Ed.), *Treatise on Geophysics (Second Edition)* (pp. 389–419). Oxford: Elsevier. https://doi.org/10.1016/B978-0-444-53802-4.00081-6

Molin, P., Acocella, V., & Funiciello, R. (2003). Structural, seismic and hydrothermal features at the border of an active intermittent resurgent block: Ischia Island (Italy). *Journal of Volcanology and Geothermal Research*, *121*(1–2), 65–81. https://doi.org/10.1016/s0377-0273(02)00412-2

Nikkhoo, M., & Walter, T. R. (2015). Triangular dislocation: an analytical, artefact-free solution. *Geophysical Journal International*, *201*(2), 1119–1141. https://doi.org/10.1093/gji/ggv035

Peregrine, D. H. (1972). Equations for Water Waves and the Approximation behind Them. In R. E. Meyer (Ed.), *Waves on Beaches and Resulting Sediment Transport* (pp. 95–121). Academic Press. https://doi.org/10.1016/B978-0-12-493250-0.50007-2

Persson, P.-O., & Strang, G. (2004). A Simple Mesh Generator in MATLAB. *SIAM Review. Society for Industrial and Applied Mathematics*, *46*(2), 329–345. https://doi.org/10.1137/s0036144503429121

Sandanbata, O., Watada, S., Satake, K., Fukao, Y., Sugioka, H., Ito, A., & Shiobara, H. (2018). Ray Tracing for Dispersive Tsunamis and Source Amplitude Estimation Based on

441 Green's Law: Application to the 2015 Volcanic Tsunami Earthquake Near Torishima,
442 South of Japan. *Pure and Applied Geophysics*, *175*(4), 1371–1385.
443 https://doi.org/10.1007/s00024-017-1746-0
444 Sandanbata, O., Kanamori, H., Rivera, L., Zhan, Z., Watada, S., & Satake, K. (2021). Moment
445 tensors of ring-faulting at active volcanoes: Insights into vertical-CLVD earthquakes at
446 the Sierra Negra caldera, Galápagos islands. *Journal of Geophysical Research, [Solid*
447 *Earth]*, *126*(6), e2021JB021693. https://doi.org/10.1029/2021jb021693
448 Sandanbata, O., Watada, S., Ho, T.-C., & Satake, K. (2021). Phase delay of short-period
449 tsunamis in the density-stratified compressible ocean over the elastic Earth.
450 *Geophysical Journal International*, *226*(3), 1975–1985.
451 https://doi.org/10.1093/gji/ggab192
452 Sandanbata, O., Watada, S., Satake, K., Kanamori, H., Rivera, L., & Zhan, Z. (2022, February
453 14). *Sub-decadal Volcanic Tsunamis Due to Submarine Trapdoor Faulting at Sumisu*
454 *Caldera in the Izu-Bonin Arc*. *Earth and Space Science Open Archive*.
455 https://doi.org/10.1002/essoar.10510526.3
456 Satake, K., & Kanamori, H. (1991). Abnormal tsunamis caused by the June 13, 1984,
457 Torishima, Japan, earthquake. *Journal of Geophysical Research*, *96*(B12), 19933–
458 19939. https://doi.org/10.1029/91jb01903
459 Shuler, A., Nettles, M., & Ekström, G. (2013). Global observation of vertical-CLVD
460 earthquakes at active volcanoes. *Journal of Geophysical Research, [Solid Earth]*,
461 *118*(1), 138–164. https://doi.org/10.1029/2012jb009721
462 Shuler, A., Ekström, G., & Nettles, M. (2013). Physical mechanisms for vertical-CLVD
463 earthquakes at active volcanoes. *Journal of Geophysical Research, [Solid Earth]*,
464 *118*(4), 1569–1586. https://doi.org/10.1002/jgrb.50131
465 Silver, P. G., & Jordan, T. H. (1982). Optimal estimation of scalar seismic moment.
466 *Geophysical Journal International*, *70*(3), 755–787. https://doi.org/10.1111/j.1365-
467 246X.1982.tb05982.x
468 Smith, I. E. M., Brothers, R. N., Muiruri, F. G., & Browne, P. R. L. (1988). The geochemistry
469 of rock and water samples from Curtis Island volcano, Kermadec group, southwest
470 Pacific. *Journal of Volcanology and Geothermal Research*.
471 https://doi.org/10.1016/0377-0273(88)90035-2
472 Takeuchi, H., & Saito, M. (1972). Seismic surface waves. *Methods in Computational Physics*,
473 *11*, 217–295.
474 Watada, S., Kusumoto, S., & Satake, K. (2014). Traveltime delay and initial phase reversal of
475 distant tsunamis coupled with the self-gravitating elastic Earth. *Journal of Geophysical*
476 *Research, [Solid Earth]*, *119*(5), 4287–4310. https://doi.org/10.1002/2013jb010841
477 Weatherall, P., Marks, K. M., & Jakobsson, M. (2015). A new digital bathymetric model of the
478 world's oceans. *Earth and Space*. https://doi.org/10.1002/2015EA000107
479 Wells, D. L., & Coppersmith, K. J. (1994). New Empirical Relationships among Magnitude,
480 Rupture Length, Rupture Width, Rupture Area, and Surface Displacement. *Bulletin of*
481 *the Seismological Society of America*, *84*(4), 974–1002.
482 https://doi.org/10.1785/BSSA0840040974
483 Yun, S.-H. (2007). *A mechanical model of the large-deformation 2005 Sierra Negra volcanic*
484 *eruption derived from InSAR measurements* (Ph.D. Dissertation). Stanford University.
485 Retrieved from https://web.stanford.edu/group/radar/people/Yun_thesis_small.pdf

Zheng, Y., Blackstone, L., & Segall, P. (2022). Constraints on absolute magma chamber volume from geodetic measurements of trapdoor faulting at Sierra Negra volcano, Galapagos. *Geophysical Research Letters*, *49*(5). https://doi.org/10.1029/2021gl095683

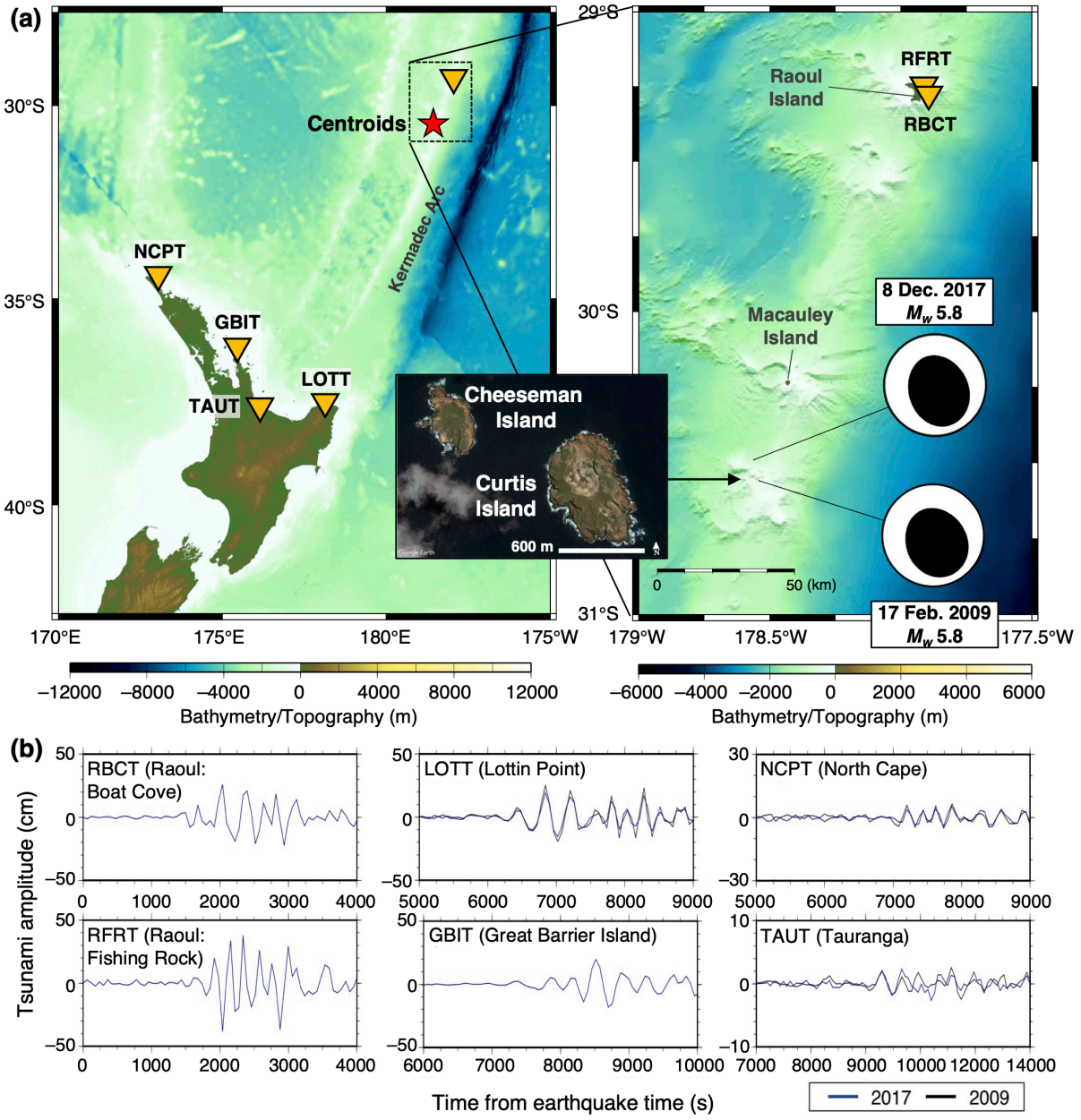

Figure 1. Curtis earthquakes. (**a**) Earthquake centroids (red star) and tide gauges (triangles). The inset figure shows a satellite image obtained from Google Earth. (**b**) Tsunami waveforms at tide gauges. Black and blue lines represent waveforms from the 2009 and 2017 earthquakes, respectively.

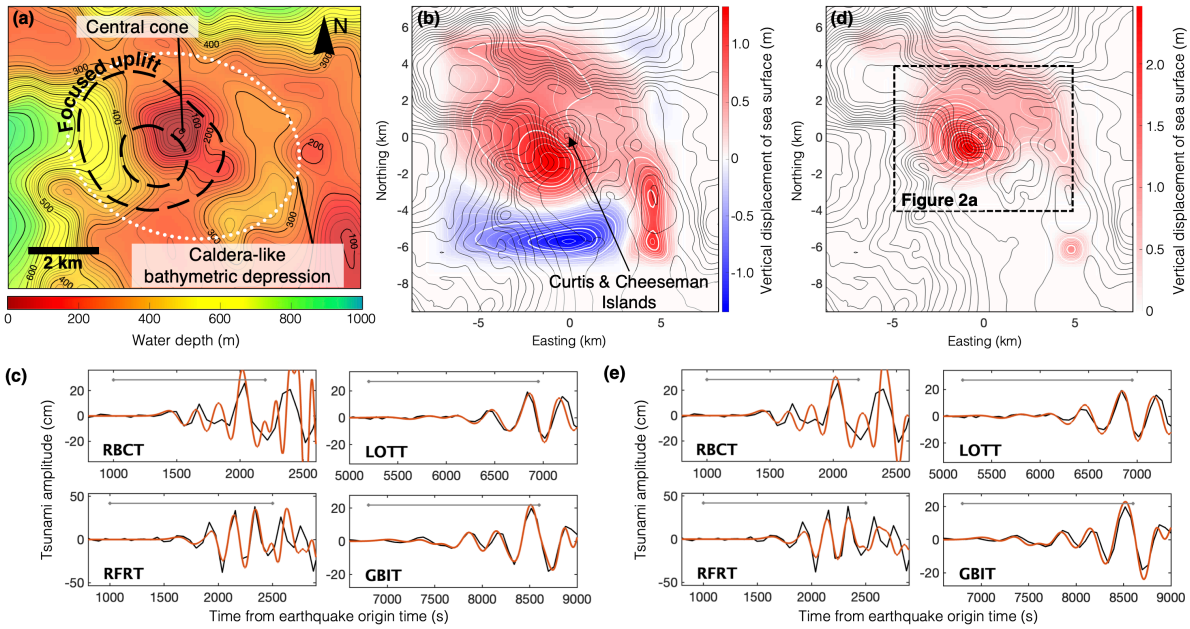

Figure 2. Vertical sea-surface displacement models for the 2017 earthquake. (**a**) Bathymetry around the islands, showing a caldera-like depression (white dashed line). Black dashed lines represent 1-m and 2-m contours of the sea-surface uplift model (shown in **d**). (**b**) Model estimated when uplift and subsidence are allowed, and (**c**) its synthetic tsunami waveforms (red) compared with observation (black) (**d**) Model estimated when only uplift is allowed, and (**e**) its synthetic tsunami waveforms. In **b** and **d**, contour lines are plotted every 50 m of water depth. In **c** and **e**, gray lines represent data lengths for the inversion. The rectangle in **d** indicates the area shown in **a**.

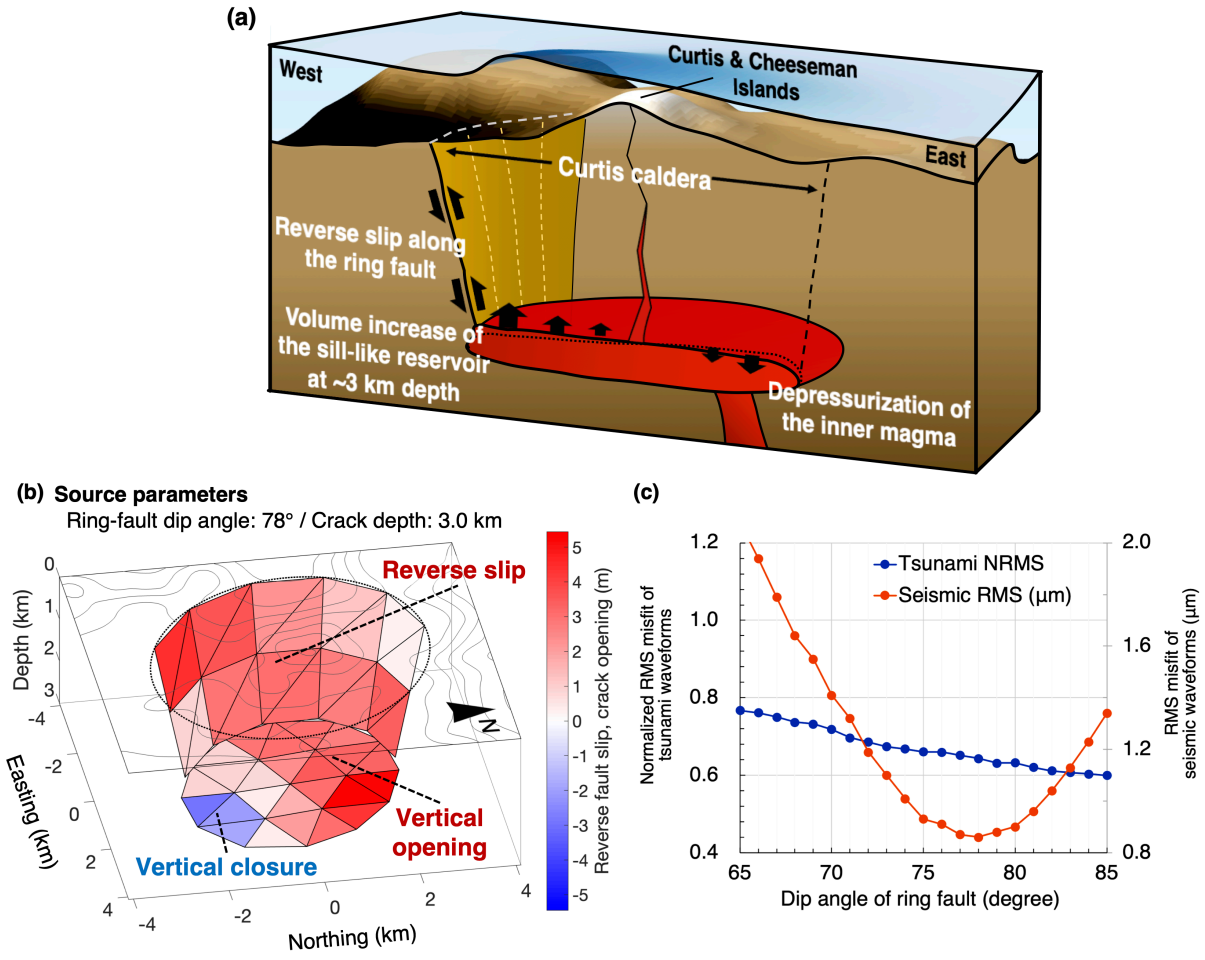

506

507 **Figure 3**. Trapdoor faulting mechanism. (**a**) Schematic illustration of the mechanism (not
508 scaled). (**b**) Our best-fit source model for the 2017 earthquake. Red color on the ring fault
509 represents reverse slip. Red and blue colors on the horizontal crack represent opening and
510 closing, respectively. (**c**) Tsunami and seismic waveform misfits for models with different dip
511 angles.

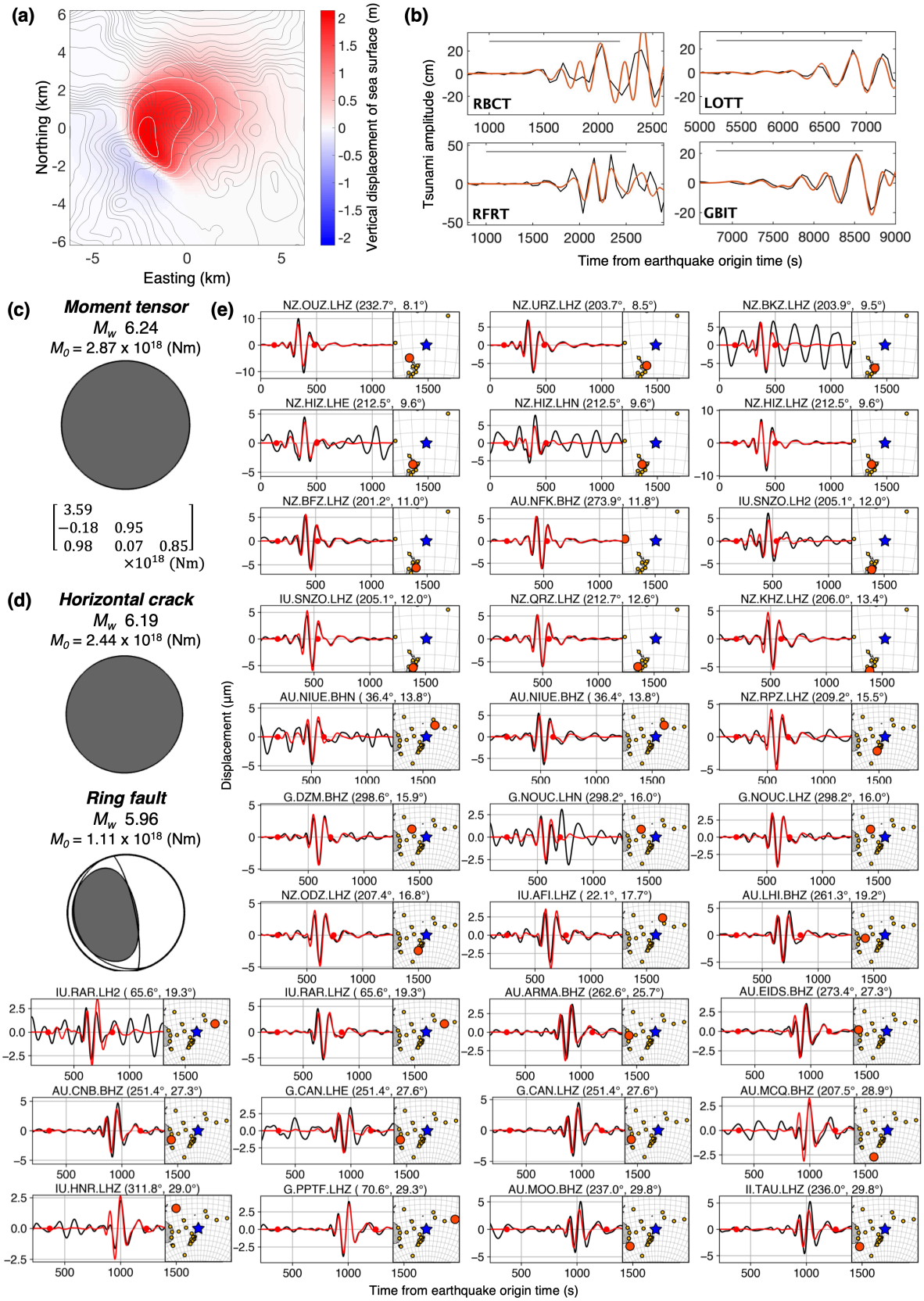
(a)
Northing (km)
Easting (km)
Vertical displacement of sea surface (m)
(b)
Tsunami amplitude (cm)
RBCT
LOTT
RFRT
GBIT
Time from earthquake origin time (s)
(c)
Moment tensor
M_w 6.24
M_0 = 2.87 x 10^{18} (Nm)
3.59
−0.18 0.95
0.98 0.07 0.85
×10^{18} (Nm)
(d)
Horizontal crack
M_w 6.19
M_0 = 2.44 x 10^{18} (Nm)
Ring fault
M_w 5.96
M_0 = 1.11 x 10^{18} (Nm)
(e)
Displacement (μm)
NZ.OUZ.LHZ (232.7°, 8.1°)
NZ.URZ.LHZ (203.7°, 8.5°)
NZ.BKZ.LHZ (203.9°, 9.5°)
NZ.HIZ.LHE (212.5°, 9.6°)
NZ.HIZ.LHN (212.5°, 9.6°)
NZ.HIZ.LHZ (212.5°, 9.6°)
NZ.BFZ.LHZ (201.2°, 11.0°)
AU.NFK.BHZ (273.9°, 11.8°)
IU.SNZO.LH2 (205.1°, 12.0°)
IU.SNZO.LHZ (205.1°, 12.0°)
NZ.QRZ.LHZ (212.7°, 12.6°)
NZ.KHZ.LHZ (206.0°, 13.4°)
AU.NIUE.BHN (36.4°, 13.8°)
AU.NIUE.BHZ (36.4°, 13.8°)
NZ.RPZ.LHZ (209.2°, 15.5°)
G.DZM.BHZ (298.6°, 15.9°)
G.NOUC.LHN (298.2°, 16.0°)
G.NOUC.LHZ (298.2°, 16.0°)
NZ.ODZ.LHZ (207.4°, 16.8°)
IU.AFI.LHZ (22.1°, 17.7°)
AU.LHI.BHZ (261.3°, 19.2°)
IU.RAR.LH2 (65.6°, 19.3°)
IU.RAR.LHZ (65.6°, 19.3°)
AU.ARMA.BHZ (262.6°, 25.7°)
AU.EIDS.BHZ (273.4°, 27.3°)
AU.CNB.BHZ (251.4°, 27.3°)
G.CAN.LHE (251.4°, 27.6°)
G.CAN.LHZ (251.4°, 27.6°)
AU.MCQ.BHZ (207.5°, 28.9°)
IU.HNR.LHZ (311.8°, 29.0°)
G.PPTF.LHZ (70.6°, 29.3°)
AU.MOO.BHZ (237.0°, 29.8°)
II.TAU.LHZ (236.0°, 29.8°)
Time from earthquake origin time (s)

513 **Figure 4**. Tsunami and long-period seismic waveforms from our source model (Figure 3b). (**a**)
514 Vertical sea-surface displacement. (**b**) Tsunami waveforms of the synthesis (red) and
515 observation (black). Gray lines represent data lengths used for the inversion. (**c**) Total moment
516 tensor of the model. (**d**) Partial moment tensors of the horizontal crack and the ring fault. (**e**)
517 Long-period seismograms of the synthesis with the model (red; moment tensor in **c**) and
518 observation (black). Red dots delimitate the data length to calculate waveform misfit. In inset
519 panels, the red circle and blue star represent the station and earthquake locations, respectively.
520 The network and station names, record component, station azimuth, and epicentral distance are
521 indicated on top.
522

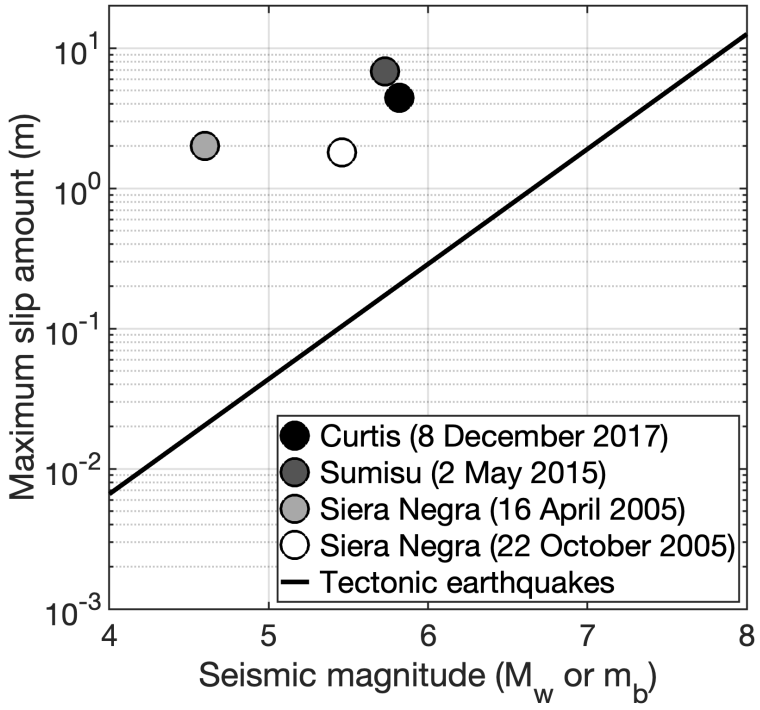

Figure 5. Earthquake scaling relationships of trapdoor faulting. Circles represent the maximum slip amount and the seismic magnitude estimated for four trapdoor faulting events at Curtis, Sumisu, and Sierra Negra. Note that the magnitude scale is m_b for the 16 April 2005 event at Sierra Negra, but M_w for the others. Black line represents the relationships for tectonic earthquakes. See text for details.

Geophysical Research Letter

Supporting Information for

Two volcanic tsunami events caused by trapdoor faulting at a submerged caldera near Curtis and Cheeseman Islands in the Kermadec Arc

Osamu Sandanbata[1,2,†], Shingo Watada[1], Kenji Satake[1], Hiroo Kanamori[3], and Luis Rivera[4]

[1]Earthquake Research Institute, the University of Tokyo, Tokyo, Japan.

[2]National Research Institute for Earth Science and Disaster Resilience, Ibaraki, Japan.

[3]Seismological Laboratory, California Institute of Technology, Pasadena, CA, USA.

[4]Université de Strasbourg, CNRS, ITES UMR 7063, Strasbourg F-67084, France.

Contents of this file

Additional Supporting Information (Files uploaded separately)

Caption for Data Set S1

Introduction

This Supporting Information contains supplementary texts, figures, and tables. In the supplementary texts (Texts S1–S6), we describe methodologies for estimation of the vertical sea-surface displacement (Text S1), earthquake source modeling (Text S2), moment tensor representation of our source model (Text S3), moment tensor analysis (Text S4), examinations of the model uniqueness (Text S5), and modeling results with either only a ring fault or only a horizontal crack (Text S6). Figures S1–S6 and Tables S1–S3 are mentioned in Main Text, while Figures S7–S17 are mentioned only in Supporting Information. Data Set S1 contains the data of the best-fit source model of the 2017 earthquake.

Text S1 Methodology for vertical sea-surface displacement modeling

S1.1 Tsunami waveform inversion for vertical sea-surface displacement

We estimate the vertical sea-surface displacement of the 2017 Curtis earthquake using a tsunami inversion method. We set a tsunami source area of 25 km × 25 km square around Curtis and Cheeseman Islands and distribute 181 unit sources of vertical sea-surface displacement with 1.25 km intervals (Figure S7), each of which is formulated as:

$$\eta^k(x,y) = 0.25 \times \left[1.0 + \cos\frac{\pi(x-x^k)}{L}\right] \times \left[1.0 + \cos\frac{\pi(y-y^k)}{L}\right], \quad \left(|x-x^k|, |y-y^k| \le L\right) \tag{S1}$$

where η^k is the vertical sea-surface displacement (in meter) of the k-th unit source ($k = 1, \dots, K$; here $K = 181$) with the central location at (x^k, y^k) (in km) with a source size of L (1.25 km, here).

We compute the Green's function $\boldsymbol{g} = g_j^k$, relating the k-th unit source to tsunami waveform at the j-th station ($j = 1, \dots, J$; here $J = 4$). We use the simulation code JAGURS (Baba et al., 2015) to solve the standard Boussinesq-type equations (Peregrine, 1972). The rise time for each unit source is assumed as 10 s, which is similar to a source duration of 6 s determined by the moment tensor analysis (see Text S4; Table S2). Bathymetry data in broad regions is modeled with GEBCO_2014 (Weatherall et al., 2015) with 30 arcsec grid spacing, and the New Zealand Regional Bathymetry with 250 m grid spacing downloaded from the National Institute of Water and Atmospheric Research (NIWA) in New Zealand. To include nearshore effects around tide gauges, we use finer bathymetry data (~28 m) obtained by combining digital topographic data on land and bathymetric data digitized and interpolated from analogue charts of the Land Information of New Zealand (LINZ) department. Because tsunami speed is reduced by the elasticity of the Earth, the compressibility and the density stratification of seawater, and the gravitational potential change due to tsunami motions (Ho et al., 2017; Sandanbata, Watada, et al., 2021; Watada et al., 2014), we approximately incorporate the effects by delaying the synthetic waveforms by 25 s at LOTT and GBIT with epicentral distances of ~830 km. The delay time is based on the estimation by Sandanbata, Watada, et al. (2021), who calculated that short-period tsunamis with a period of 500 s in water of 1-km depth are delayed by about 3 s every 100-km distance.

We then solve the observation equation by the damped least-squares method (pp. 695–699 in Aki & Richards [1980]):

$$\begin{bmatrix} \boldsymbol{d} \\ \boldsymbol{0} \end{bmatrix} = \begin{bmatrix} \boldsymbol{g} \\ \alpha \boldsymbol{I} \end{bmatrix} \boldsymbol{m}, \tag{S2}$$

where $\boldsymbol{d} = [d_1(t) \quad \dots \quad d_J(t)]^T$ is the column vector of the observed tsunami data at the j-th station, $\boldsymbol{g} = \begin{bmatrix} g_1^1(t) & \cdots & g_1^K(t) \\ \vdots & \ddots & \vdots \\ g_J^1(t) & \cdots & g_J^K(t) \end{bmatrix}$ is the Green's function, $\boldsymbol{m} = [m^1 \quad \dots \quad m^K]^T$ is an unknown column vector of the amplitude factor of the k-th unit source, $\boldsymbol{I}$ is the identity matrix, and α is the damping parameter to obtain a smooth source model, which we

assume as 0.02. We set data length to include several wave crests and troughs of the tsunami signal. By the superposition of the unit sources η^k weighted by m_i^k, we obtain the vertical sea-surface displacement model. Additionally, we obtain an uplift source model without subsidence, by solving Equation S2 with the non-negative condition (i.e., $\boldsymbol{m} \geq \mathbf{0}$).

S1.2. Resolution tests

Our modeling is mainly based on tsunami data from the tide gauge records with a low sampling rate (one sample per 60 s) and limited azimuthal coverage of stations. To investigate the resolution of our tsunami waveform inversion, we conduct two resolution tests, in which we prepare two target models: (1) a checker-board distribution (Figure S8a), and (2) an uplift distribution near Curtis caldera (Figure S9a). Synthetic tsunami waveforms from the two target models are computed by the tsunami simulation method explained in Text S1.1, and resampled with a time interval of 60 s; additionally, the waveforms of LOTT and GBIT are delayed by 25 s. We then apply the tsunami waveform inversion to these synthetic waveform data.

For the checker-board distribution (Figure S8a), the tsunami waveform inversion yields a solution (Figure S8b), which is somewhat different from the target, although the target waveforms are reproduced well (Figure S8c). This shows that complex distribution patterns near the caldera can be poorly constrained from our inversion based on the tide-gauge tsunami data. On the other hand, the inversion for the uplift distribution near the caldera (Figure S9a) yields uplift distribution over the caldera similar to the target model (Figure S9b), reproducing the target waveforms (Figure S9c). We note that the peak location is estimated well, while the horizontal size and amplitude are estimated with slight difference.

These results suggest that, although our inversion cannot resolve complex pattern of sea-surface displacement, a simple-shaped displacement focused near the caldera can be resolved well with good resolutions on its location and overall shape. We emphasize that the observed tsunami waveforms have long-period characters (Figure 1b in Main Text) and are similar to the waveforms computed from the uplift distribution (Figure S9c) rather than those from the checker-board distribution (Figure S8c). This indicates that the actual sea-surface displacement caused by the earthquake and the uplift distribution were alike (Figure S9a); this was also proposed by Gusman et al. (2020). Therefore, it is plausible to consider that our vertical displacement models with a localized uplift in the western part of the caldera, which are estimated in Section 4.1 (Figures 2b and 2d) in Main Text, reasonably reflect the actual sea-surface displacement due to the earthquake.

Text S2 Methodology for earthquake source modeling

S2.1 Source structures of the fault-crack composite source system

We assume a fault-crack composite source system, composed of an inward-dipping ring fault connected to a horizontal crack at a depth of 3 km in the crust, which is discretized with triangular meshes (Figure S1). Given the focused uplift estimated in Section 4.1 in Main Text, we assume a partial ring fault on the western side of the caldera with a central angle of 150° that extends from the seafloor to the crack edge. Although the detailed

geometry is unknown, the ring fault is assumed to be along an elliptical line; this ellipse is with the center at (178.56°W, 30.542°S), the major axis oriented S60°E, and the horizontal size of 3.4 km × 2.8 km on the seafloor. For the ring fault, we assume a uniform inward dip angle, varied from 65° to 85°. Only inward dip angles are considered, because the vertical-T CLVD moment tensor can be generated when the caldera floor uplifts along with an inward-dipping ring fault (see Figure 1 in Sandanbata, Kanamori, et al. 2021; Figure 9 in Shuler, Ekström, et al., 2013). Thus, we prepare tens of source structures with different ring-fault dip angles.

We discretize the source system into triangular source elements. The ring fault is divided into elements with an arc angle of 30° along the circumference and 1.5 km along the depth, and a trapezoid composed of two neighboring triangular elements with the same dip and strike angles is considered as a sub-fault. The horizontal crack is discretized using the DistMesh code (Persson & Strang, 2004), each of which is considered as sub-crack. By a tsunami waveform inversion explained later, we will determine amounts of the reverse slip of each sub-fault and the opening/closure of each sub-crack, denoted by $\boldsymbol{s} = [s_1 \quad \cdots \quad s_{N_s}]^T$ and $\boldsymbol{\delta} = [\delta_1 \quad \cdots \quad \delta_{N_\delta}]^T$, respectively. Because the dislocations of the ring fault and the horizontal crack should be similar to each other at their contacts, we link the vertical component of the sub-fault slip at bottom to the sub-crack opening/closing at edge adjacent to the sub-fault by imposing a kinematic condition:

$$s_p \sin \Delta_p = \delta_q \tag{S3}$$

where Δ_p is the dip angle of the p-th sub-fault to which the q-th sub-crack is adjacent.

S2.2 Tsunami waveform inversion of dislocations of the fault-crack composite source

For each source structure assumed above, we perform a tsunami waveform inversion to obtain a fault-crack composite source model. We use the same tsunami data, as described in Section 3.1 of Main Text.

To efficiently compute the Green's function relating each sub-fault slip or sub-crack opening to the tsunami waveforms, we use the method proposed in a previous study (Sandanbata et al., 2022), which is summarized as follows. First, we compute the vertical sea-surface displacement excited by unit dislocation of the i-th source element (i.e., 1-m reverse slip of sub-fault or 1-m vertical opening of sub-crack; $i = 1, \ldots, I$; here I depend on source structure). We calculate vertical *seafloor* displacement due to each source element by the triangular dislocation method (Nikkhoo & Walter, 2015) assuming flat seafloor and Poisson's ratio of 0.25, and we convert it into vertical *sea-surface* displacement by applying the Kajiura's filter (Kajiura, 1963). The water depth of 400 m is used for this filter. We thus compute the sea-surface displacement from the i-th source element $h_i(x, y)$. Second, we approximate the vertical sea-surface displacement $h_i(x, y)$ of the i-th source element by a linear combination of the unit sources $\eta^k(x, y)$ used in Section 4.1 of Main Text and Text S1 (Equation S1; Figure S7):

$$h_i(x, y) \approx \sum_{k=1}^{K} m_i^k \eta^k(x, y), \tag{S4}$$

where the amplitude factors m_i^k are obtained by a least-squares method. Third, we compute the Green's functions relating the i-th source element to the tsunami data at the j-th station by superimposing the Green's functions of the unit sources g_j^k multiplied by the amplitude factors m_i^k:

$$G_{ij}(t) = \sum_k m_i^k g_j^k(t). \quad \text{(S5)}$$

Finally, to obtain a source model, we determine the dislocations of the fault-crack composite source system by solving the observation equation with the damped least-squares method:

$$\begin{bmatrix} \boldsymbol{d} \\ \boldsymbol{0} \\ \boldsymbol{0} \end{bmatrix} = \begin{bmatrix} \boldsymbol{G} \\ \boldsymbol{K} \\ \beta \boldsymbol{I} \end{bmatrix} \begin{bmatrix} \boldsymbol{s} \\ \boldsymbol{\delta} \end{bmatrix}, \quad \text{(S6)}$$

where $\boldsymbol{d}$ is the observed tsunami data at the j-th station, and $\boldsymbol{G} = \begin{bmatrix} G_{11}(t) & \cdots & G_{I1}(t) \\ \vdots & \ddots & \vdots \\ G_{1J}(t) & \cdots & G_{IJ}(t) \end{bmatrix}$ is the matrix of the Green's functions G_{ij}. $\boldsymbol{s}$ is an unknown column vector of reverse slip amounts for sub-faults, for which we impose the non-zero condition ($\boldsymbol{s} \geq \boldsymbol{0}$), and $\boldsymbol{\delta}$ is an unknown column vector of opening amounts for sub-cracks, for which we allow either positive (opening) or negative (closing) values. The linear equation of $\boldsymbol{K}\begin{bmatrix} \boldsymbol{s} \\ \boldsymbol{\delta} \end{bmatrix} = \boldsymbol{0}$ represents the kinematic condition of Equation S3. β is the damping parameter, which we set at 0.015 by taking a balance between the solution smoothness and the waveform fit (Figure S10).

To evaluate the waveform fit between the observed tsunami waveforms and synthetic waveforms from an obtained source model, we quantify the normalized root-mean-square (NRMS) misfit of the tsunami waveforms, which we call *tsunami NRMS misfit*:

$$\sqrt{\sum_j \left\| \boldsymbol{c}_j^t - \boldsymbol{d}_j^t \right\|^2 / \sum_j \left\| \boldsymbol{c}_j^t \right\|^2}, \quad \text{(S7)}$$

where $\boldsymbol{c}_j^t$ and $\boldsymbol{d}_j^t$ are the observed waveform and synthetic waveforms within the inversion time window at the j-th station, respectively. $\| \ \|$ denotes the L2 norm of data vector.

S.2.3 Forward computation of long-period seismic waveforms

For validation of fault-crack composite source models obtained by the tsunami waveform inversion, we compute long-period seismic waveforms from the source models and compare them with the seismic data. The moment tensor of the models $\boldsymbol{M}$ is written by:

$$\boldsymbol{M} = \boldsymbol{M}_{RF} + \boldsymbol{M}_{HC} = \sum \boldsymbol{m}_{RF}^p + \sum \boldsymbol{m}_{HC}^q, \quad \text{(S8)}$$

where $\boldsymbol{M}_{RF}$ and $\boldsymbol{M}_{HC}$ represent moment tensors of the ring fault and the horizontal crack, respectively, and $\boldsymbol{m}_{RF}^p$ and $\boldsymbol{m}_{HC}^q$ are moment tensors of the p-th sub-fault and the q-th sub-crack, respectively. We compute $\boldsymbol{m}_{RF}^p$ with the slip amount and strike, dip, and rake (90°) angles (Box 4.4 in Aki & Richards, 1980), with the seismic moment of $\mu s_p A_p$, where s_p and A_p are slip amount and area, respectively, and μ is rigidity, or Lamé's constant. We calculate $\boldsymbol{m}_{HC}^q$ by:

$$\boldsymbol{m}_{HC}^{q} = \begin{bmatrix} M_{rr} & M_{\theta r} & M_{\phi r} \\ M_{r\theta} & M_{\theta\theta} & M_{\phi\theta} \\ M_{r\phi} & M_{\theta\phi} & M_{\phi\phi} \end{bmatrix} = \delta_q \times A_q \times \begin{bmatrix} \lambda + 2\mu & 0 & 0 \\ 0 & \lambda & 0 \\ 0 & 0 & \lambda \end{bmatrix}, \quad \text{(S9)}$$

where δ_q and A_q are the opening amount and area, respectively (Kawakatsu & Yamamoto, 2015). We assume Lamé's constants of λ and μ as 34.2 GPa, and 26.6 GPa, respectively, calculated with the P- and S-wave velocities and the density in the shallowest crust layer of 1-D Preliminary Reference Earth Model (PREM) (Dziewonski & Anderson, 1981). The total seismic moment is calculated by

$$M_0 = \sqrt{\Sigma_{ij} M_{ij} M_{ij}/2}, \quad \text{(S10)}$$

(pp. 166–167 in Dahlen & Tromp, 1998; Silver & Jordan, 1982) and the moment magnitude by

$$M_w = \frac{2}{3}(\log_{10} M_0 - 9.10), \quad \text{(S11)}$$

with M_0 in the N m scale (Hanks & Kanamori, 1979; Kanamori, 1977).

Using the W-phase package (Duputel et al., 2012; Hayes et al., 2009; Kanamori & Rivera, 2008), we compute long-period seismic waveforms from the moment tensor $\boldsymbol{M}$. Green's functions of seismic waves are calculated with the PREM model by the normal mode method (Takeuchi & Saito, 1972). The centroid is at the center of Curtis caldera (178.56°W, 30.54°S) and at the depth of 0.5 km below the seafloor. Both the half duration and the centroid time shift are assumed to be 5 s, which are comparable to the values (3 s and 3 s, respectively) obtained by the moment tensor inversion (Text S4; Table S3). We apply the same filter to the synthetic waveforms, as used for the seismic data.

To quantify the seismic waveform fit, we calculate the root-mean-square (RMS) misfit of the seismic waveforms, which we call *seismic RMS misfit*:

$$\sqrt{\Sigma_j \left\| \boldsymbol{c}_j^s - \boldsymbol{d}_j^s \right\|^2}, \quad \text{(S12)}$$

where $\boldsymbol{c}_j^s$ and $\boldsymbol{d}_j^s$ are the synthetic and observed seismic waveforms at the j-th station. The data length for this calculation includes P, S, and surface waves.

Text S3 Contribution to long-period seismic waves

The moment tensor of our best-fit source model $\boldsymbol{M}$ is highly isotropic with M_w 6.24 (Figure 4c in Main Text), whereas the deviatoric moment tensor of the 2017 Curtis earthquake reported in the GCMT catalogue is a vertical-T CLVD type with M_w 5.8 (Figure 1a in Main Text). Here we discuss the reason for the differences between the moment tensors. Figure S5a shows synthetic seismograms at representative stations from the moment tensor $\boldsymbol{M}$ (= $\boldsymbol{M_{HC}}$ + $\boldsymbol{M_{RF}}$) of our model. For comparison, we show synthetic seismograms from moment tensors of the horizontal crack $\boldsymbol{M_{HC}}$ and the ring fault $\boldsymbol{M_{RF}}$ in Figures S5b and S5c, respectively. Although $\boldsymbol{M_{HC}}$ has a larger moment magnitude (M_w 6.19) than $\boldsymbol{M_{RF}}$ (M_w 5.96), the seismic amplitudes from $\boldsymbol{M_{HC}}$ are much smaller than those from $\boldsymbol{M_{RF}}$. This is because the vertical motion of a horizontal crack at a very shallow depth has only a low efficiency

of long-period seismic radiation (Fukao et al., 2018; Sandanbata, Kanamori, et al., 2021). Note that the polarities of seismograms from $\boldsymbol{M_{HC}}$ are reversed to those from $\boldsymbol{M_{RF}}$, which is known as the trade-off between the vertical-CLVD and isotropic components at shallow depth (Kawakatsu, 1996; Sandanbata, Kanamori, et al., 2021; compare Figures S5b and S5c). Hence, $\boldsymbol{M_{HC}}$ slightly reduces the seismic amplitudes from $\boldsymbol{M}$ but does not change the waveform shapes much.

To further examine radiations from the ring fault, we show in Figure S5d synthetic seismograms from $\boldsymbol{M_{RF}}$ excluding two elements representing vertical dip-slip, $M_{r\theta}$ and $M_{r\varphi}$ (i.e., from M_{rr}, $M_{\theta\theta}$, $M_{\varphi\varphi}$, and $M_{\theta\varphi}$ of $\boldsymbol{M_{RF}}$). Although the moment magnitude decreases by 0.2 compared to that of $\boldsymbol{M_{RF}}$, the synthetic seismograms are very similar to those from $\boldsymbol{M_{RF}}$. This demonstrates that the two excluded elements, $M_{r\theta}$ and $M_{r\varphi}$, at a very shallow depth are very inefficient in radiating long-period seismic waves (Sandanbata, Kanamori, et al., 2021). Hence, long-period seismic waves of the earthquakes mainly arise from the four elements, M_{rr}, $M_{\theta\theta}$, $M_{\varphi\varphi}$, and $M_{\theta\varphi}$, of $\boldsymbol{M_{RF}}$. This moment tensor composed of the four elements is a vertical-T CLVD type, which is very similar to the GCMT solution (Figure 1a in Main Text).

Text S4 Moment tensor analysis

We use the W-phase code (Duputel et al., 2012; Hayes et al., 2009; Kanamori & Rivera, 2008) to perform the deviatoric moment tensor (MT) inversion analysis for the 2009 and 2017 earthquakes using long-period seismic data. This analysis is independent of the source modeling in Main Text. For the two earthquakes, we download seismic records of LH and BH channels at stations within 5°–30° from seismic networks (network codes: II, IU, AU, NZ, and G). For computation of the Green's function of seismic waveforms, we use the normal mode method (Takeuchi & Saito, 1972) with the 1-D Preliminary Reference Earth Model (PREM) (Dziewonski & Anderson, 1981). The time window includes P, S, and surface waves. We impose the zero-trace constraint, $M_{rr} + M_{\theta\theta} + M_{\varphi\varphi} = 0$. We assume the centroid location at (178.56°W, 30.54°S) and the depth at 2.5 km in the crust, and apply the same filter, as done in the source modeling (see Text S2.3). We start the inversion with a half duration t_h and a centroid time shift t_c reported in the GCMT catalog, and grid-search optimal values for $t_h = t_c$. During the inversion process, we select seismic data yielding a single-record normalized root-mean-square (NRMS) misfit ≤ 1.0, which is calculated by $\sqrt{\|\boldsymbol{c}_i^s - \boldsymbol{d}_i^s\| / \|\boldsymbol{c}_i^s\|}$, where $\boldsymbol{c}_i^s$ and $\boldsymbol{d}_i^s$ are synthetic and observed data in the inversion window at the i-th station, respectively. The selected datasets are composed of 29 and 33 records of the 2009 and 2017 earthquakes, respectively (Figures S11 and S12).

Table S3 shows the obtained deviatoric moment tensor of the 2009 and 2017 earthquakes. The seismic moment and moment magnitude of the two earthquakes are much larger than those in the GCMT catalogue (Table S1), because for such shallow earthquakes $M_{r\theta}$ and $M_{r\varphi}$ cannot be estimated accurately (Kanamori & Given, 1981; Sandanbata, Kanamori, et al., 2021).

Following a previous study (Sandanbata, Kanamori, et al., 2021), we estimate the ring-fault geometries of the 2009 and 2017 earthquakes using *resolvable moment tensor* $\boldsymbol{M_{res}}$. We obtain $\boldsymbol{M_{res}}$ by removing $M_{r\theta}$ and $M_{r\varphi}$ from the estimated deviatoric moment tensor, decompose $\boldsymbol{M_{res}}$ into two components, i.e., vertical-CLVD component $\boldsymbol{M_{CLVD}}$ and vertical strike-slip component $\boldsymbol{M_{SS}}$, and calculate the moment ratio of $\boldsymbol{M_{CLVD}}$ to $\boldsymbol{M_{SS}}$, or the CLVD ratio k_{CLVD}. Figure S6 shows thus-obtained $\boldsymbol{M_{res}}$ and the CLVD ratios of the two earthquakes. Using the relationships between the Null-axis direction of $\boldsymbol{M_{res}}$ and the ring-fault orientation, and between k_{CLVD} and the arc angle of the ring fault (see Figure 4 in Sandanbata, Kanamori, et al., 2021), we estimate that the 2009 and 2017 earthquakes occurred with ring faults with arc angles of ~100° and ~120°, respectively, both of which are oriented in the NNW–SSW direction.

Text S5 Examinations of the uniqueness of the source geometry

To examine the uniqueness of our source model proposed in Section 4.2 in Main Text, we additionally perform the source modeling with some modifications in geometries, and assumption of the fault-slip direction.

S5.1 Source geometry

We examine how the source geometries of trapdoor faulting, i.e., crack depth and ring-fault length, are constrained by our analysis. As proposed below, models with slightly different geometries can explain the tsunami and seismic data overall, suggesting that our analysis have only weak constraints on the two parameters.

(1) Depth of a horizontal crack

We first test a fault-crack composite source system with a deeper horizontal crack at a depth of 6 km in the crust (Figure S13). The tsunami waveform inversion yields a dislocation pattern of the fault-crack source system (Figure S13a) similar to that presented in our main results (Figure 3b in Main Text), and the tsunami waveform fit is overall good (tsunami NRMS of 0.74; Figure S13b). Long-period seismic waveforms computed with this model also show good agreements with the observed seismic data (seismic RMS of 0.96 μm; Figure S13e).

(2) Length of a ring fault

We also test a fault-crack source system with a longer ring fault (with a central angle of 240°), as shown in Figure S14a. The modeling results show that the estimated dislocations of the source system support the trapdoor faulting mechanism, and the tsunami and seismic waveform data are explained sufficiently (the tsunami NRMS of 0.68 and seismic RMS of 0.91 μm; Figures S14b and S14e).

S5.2 Slip direction of a ring fault

In Main Test, we assume only reverse slip on the ring fault. Here, we instead assume a fully elliptic ring fault and perform the tsunami waveform inversion by allowing both reverse and normal slips on the ring fault. In this case, we obtain a source model that contains reverse slips on the northern, western, and southern faults but normal slip on the eastern

fault, as shown in Figure S15a. This model can explain the tsunami and seismic data overall, with a tsunami NRMS of 0.68 and seismic RMS of 0.97 μm; Figure S15b and S15e). This suggests that the trapdoor faulting perhaps involved normal faulting associated with the magma flow within the crack, but our analysis cannot determine whether a fault on the eastern side slipped or not.

Text S6 Models of only a ring fault or only a horizontal crack

We test if the fault-crack composite source model is preferable to models of only a ring fault or only a horizontal crack. We conduct the source modeling by assuming only a fully elliptical ring fault (with reverse slip), or only a horizontal crack (with vertical opening or closure), as shown in Figures S16 and S17, respectively. The model of only a ring fault explains the tsunami waveform data worse (Figure S16b), while the long-period seismic data are well explained (Figure S16c). On the other hand, the horizontal crack opening alone reproduces the tsunami data well (Figures S17b), but the model excites far smaller-amplitude seismic waves with flipped polarities compared to those of the observed waveforms (Figures S17c). These suggest that our model combining a ring fault and a horizontal crack is more plausible for the earthquake source model, compared to only a ring-faulting or only a crack opening.

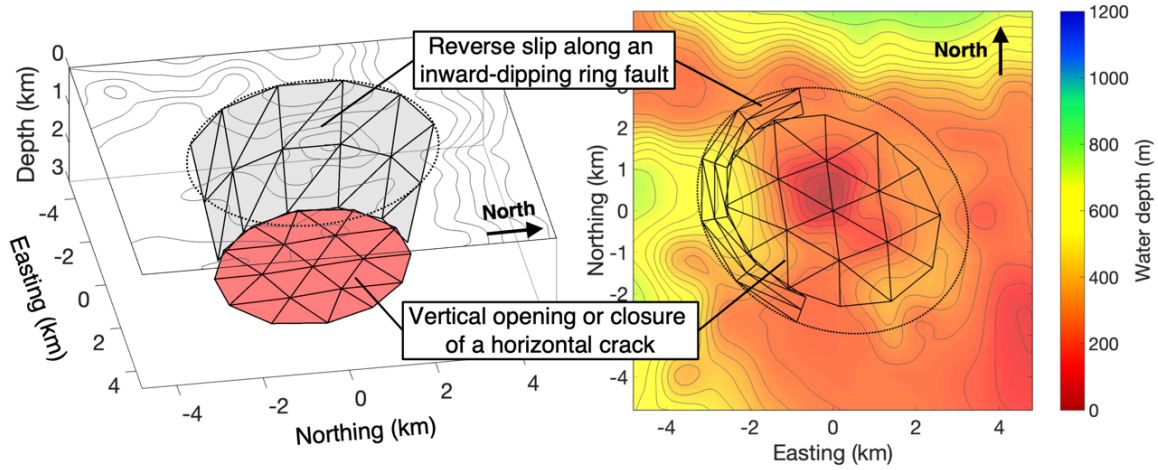

Figure S1. An assumed fault-crack composite source system, composed of a partial ring fault and a horizontal crack, viewed from the east (left) and above (right). This structure is discretized into triangular meshes.

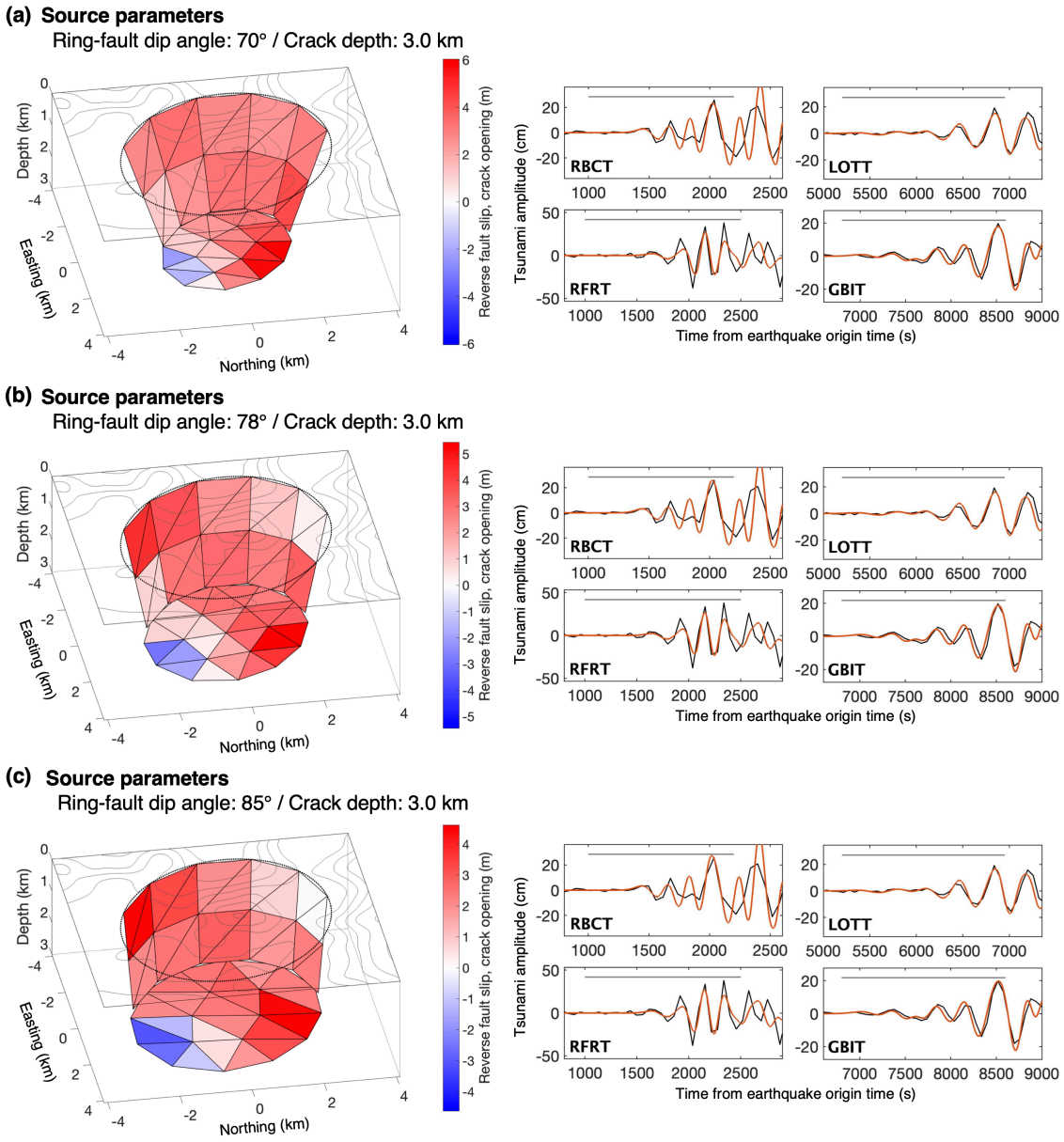

Figure S2. Source models with different ring-fault dip angles: (**a**) 70°, (**b**) 78°, and (**c**) 85°. All the models have a horizontal crack at a depth of 3 km in the crust. (Left) Dislocations of the fault-crack source system determined by the tsunami waveform inversion. See the caption of Figure 3b in Main Text. (Right) Synthetic tsunami waveforms from this model (red), compared with observed waveforms (black). See the caption of Figure 4b in Main Text. Note that variations of the ring-fault dip angle do not change the tsunami waveforms.

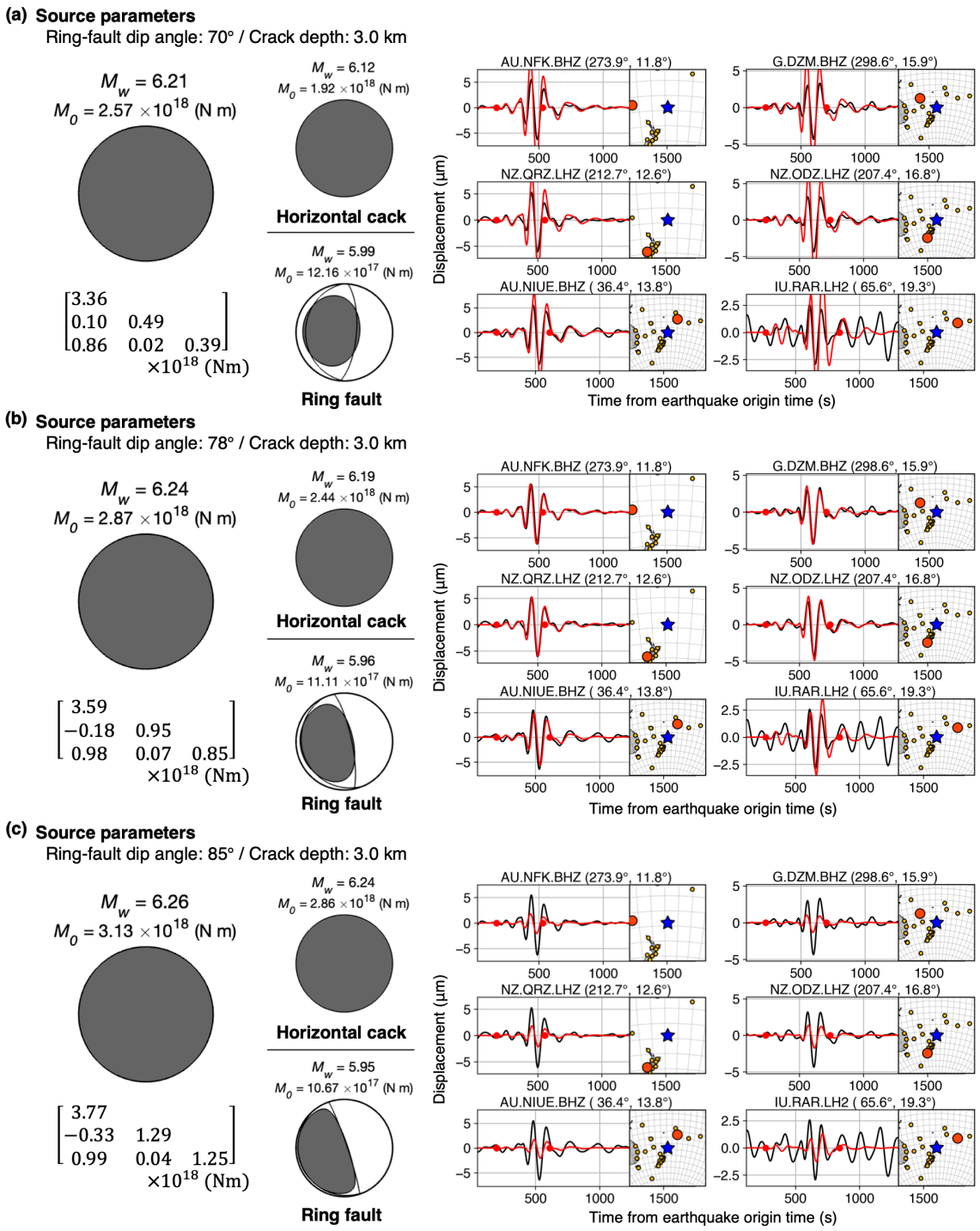

Figure S3. Moment tensors and seismic waveforms from the source models with a dip angle of (**a**) 70°, (**b**) 78°, and (**c**) 85°; all these models have a horizontal crack at a depth of 3 km in the crust, which are shown in Figure S2. Partial moment tensors of the horizontal crack and the ring fault are shown with the moment tensor of the model. Red and black lines represent synthetic and observed waveforms, respectively. Note that variations of the ring-fault dip angle change the seismic wave amplitudes largely.

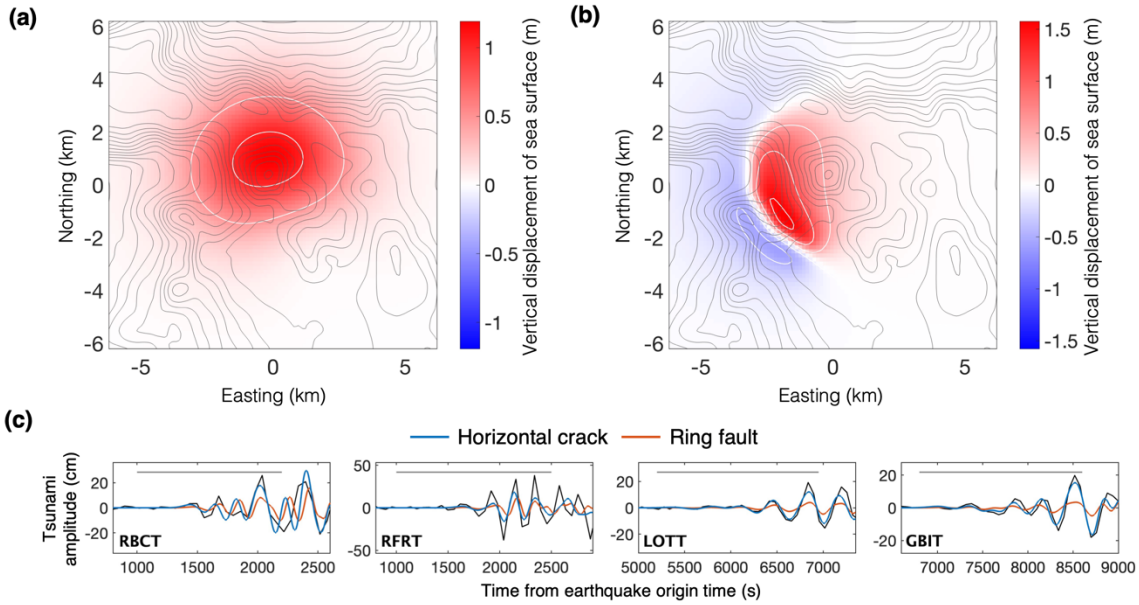

Figure S4. Contributions to tsunami waves by the horizontal crack and the ring fault of the best-fit source model (Figure 3b in Main Text). (**a**–**b**) Vertical sea-surface displacements caused by (**a**) the horizontal crack and (**b**) the ring fault. Red and blue colors represent uplift and subsidence, respectively, with white contour lines plotted every 0.5 m. (**c**) Comparison of the synthetic tsunami waveforms from the horizontal crack (blue) and the ring fault (red), compared with the observed (black) waveforms. The gray line represents the time interval used for the inversion.

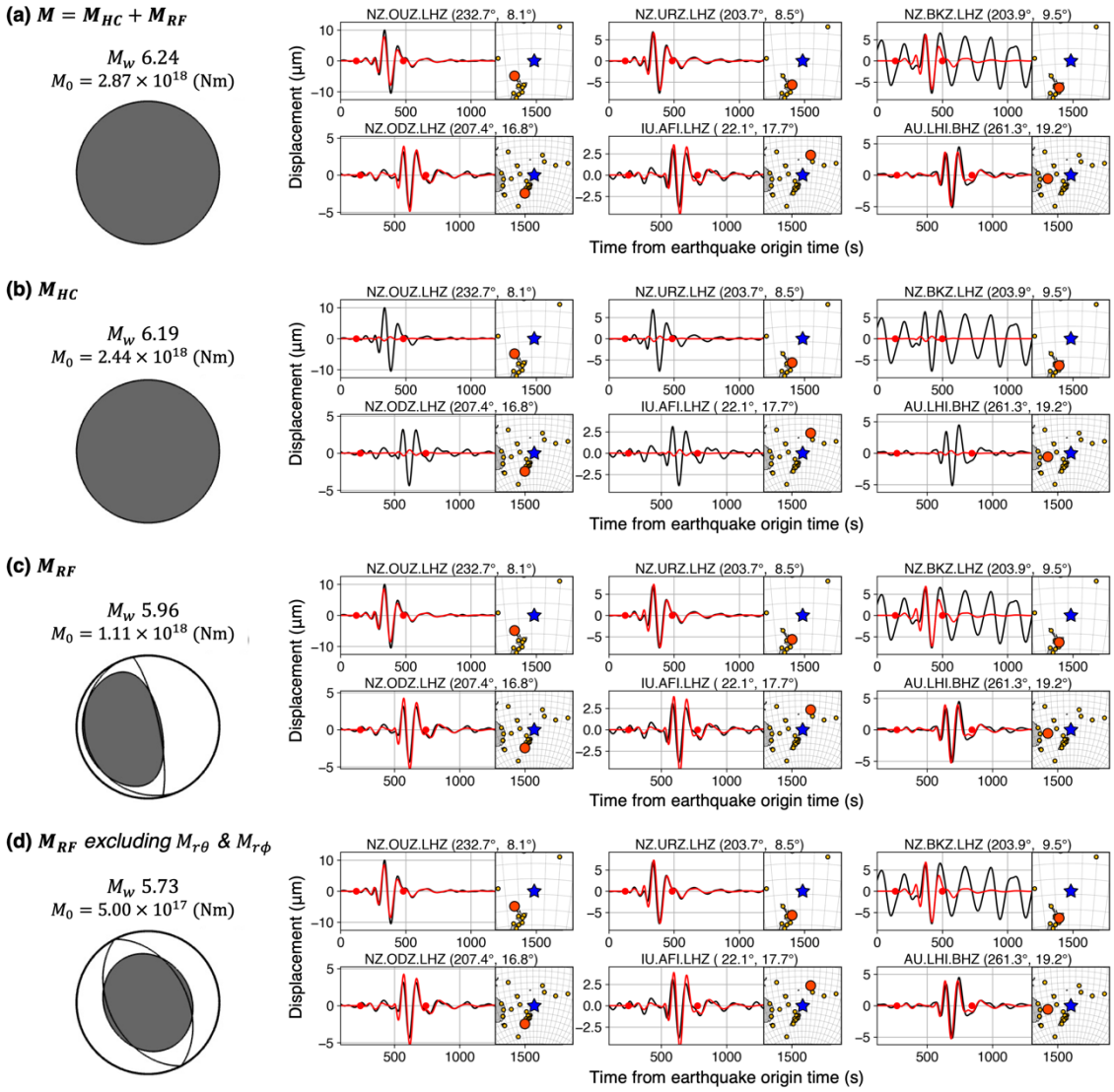

Figure S5. Contributions to long-period seismic waves by the best-fit source model (Figure 3b in Main Text). Red lines in the right panels represent synthetic waveforms from (**a**) $\boldsymbol{M}$ (= $\boldsymbol{M_{HC}}$ + $\boldsymbol{M_{RF}}$), the partial moment tensors of (**b**) the horizontal crack $\boldsymbol{M_{HC}}$ and (**c**) the ring fault $\boldsymbol{M_{RF}}$, and (**d**) the moment tensor of the ring fault, excluding $M_{r\theta}$ and $M_{r\varphi}$. Note that that the smaller-amplitude waveforms from $\boldsymbol{M_{HC}}$ have the reversed polarities relative to those from $\boldsymbol{M_{RF}}$, reducing the seismic amplitudes of $\boldsymbol{M}$, and that the main contributor to the long-period seismic waves is the limited moment-tensor components shown in **d**.

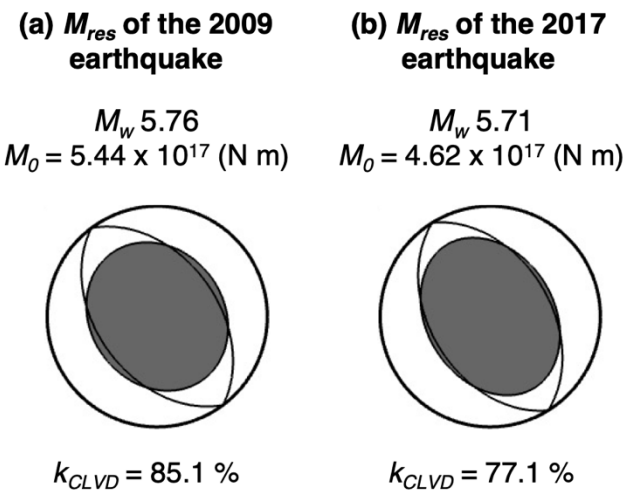

Figure S6. Resolvable moment tensors $\boldsymbol{M_{res}}$ of the (**a**) 2017 and (**b**) 2009 Curtis earthquakes determined by the moment tensor analysis (see Text S4). The orientation of the best double-couple solution is shown by thin curves, whose Null-axis direction coincides with that of $\boldsymbol{M_{res}}$. The focal mechanisms are shown by projection of the lower focal hemisphere.

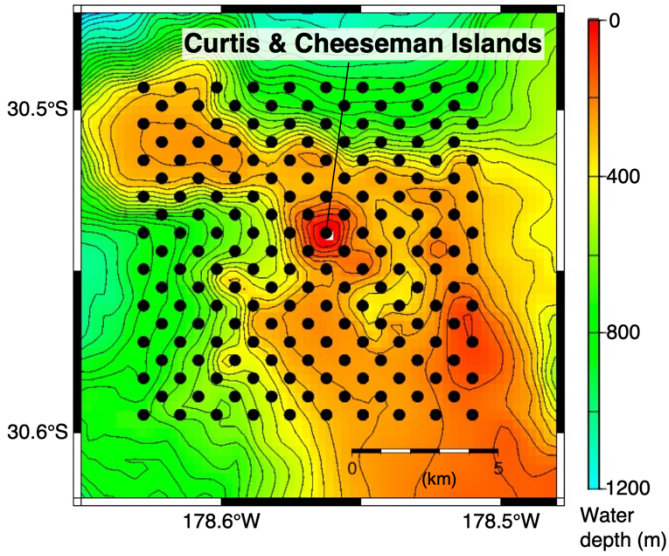

Figure S7. Unit sources of vertical sea-surface displacement around Curtis & Cheeseman Islands. Black dots represent central locations of the unit sources. Each unit source has a cosine-tapered shape with a horizontal source size of 1.25 km x 1.25 km. Contour lines of the water depth are plotted every 50 m.

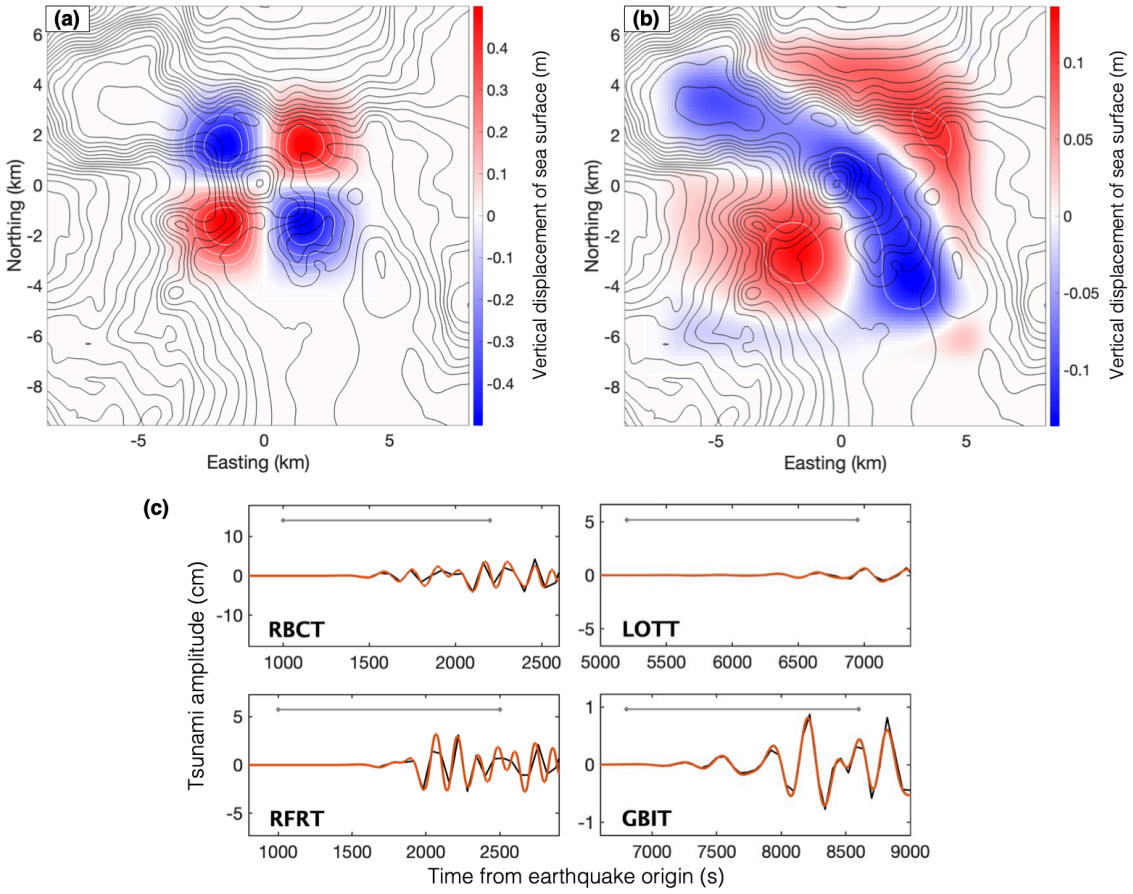

Figure S8. Resolution test of the tsunami waveform inversion for vertical sea-surface displacement: a case of a checker-board distribution. (**a**) Target model, and (**b**) inverted model. (**c**) Synthetic tsunami waveforms from the target (red) and inverted models (black). The gray line represents the time interval used for the inversion.

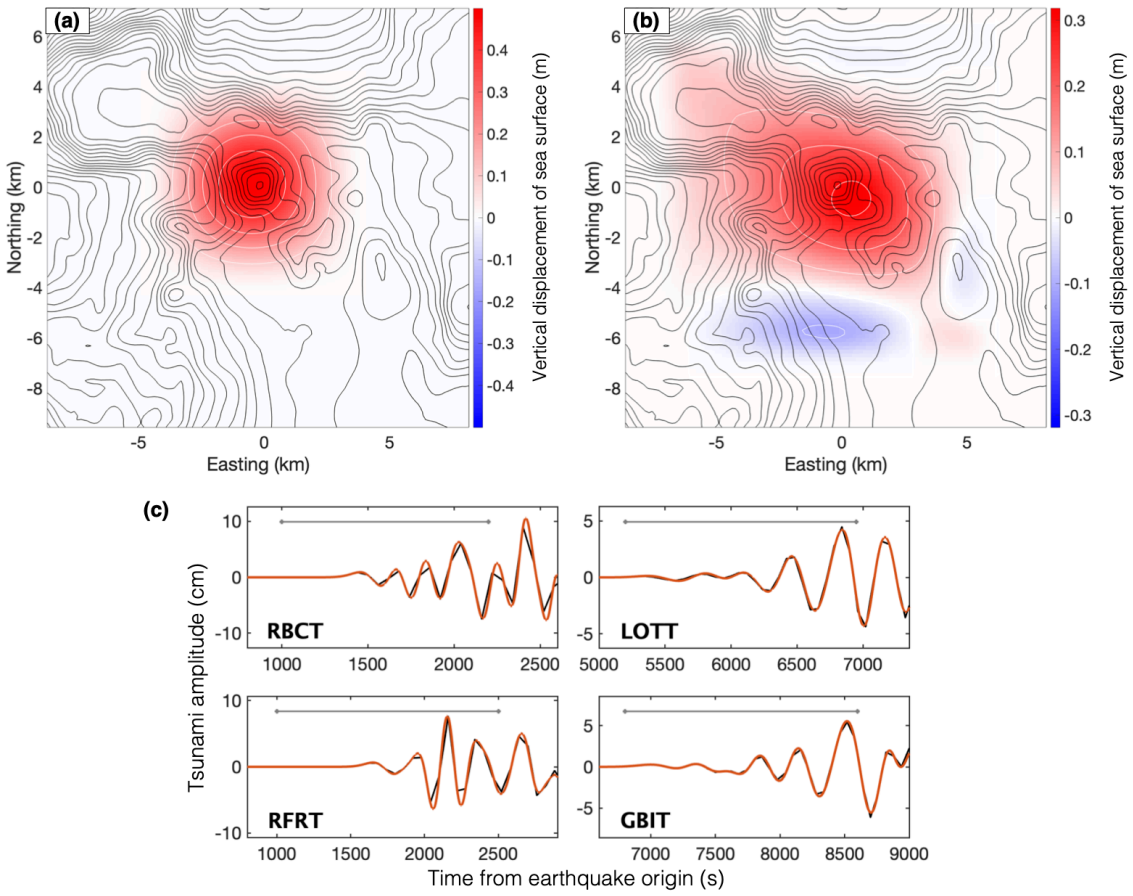

Figure S9. Same as Figure S8, but for a case of an uplift distribution near Curtis caldera.

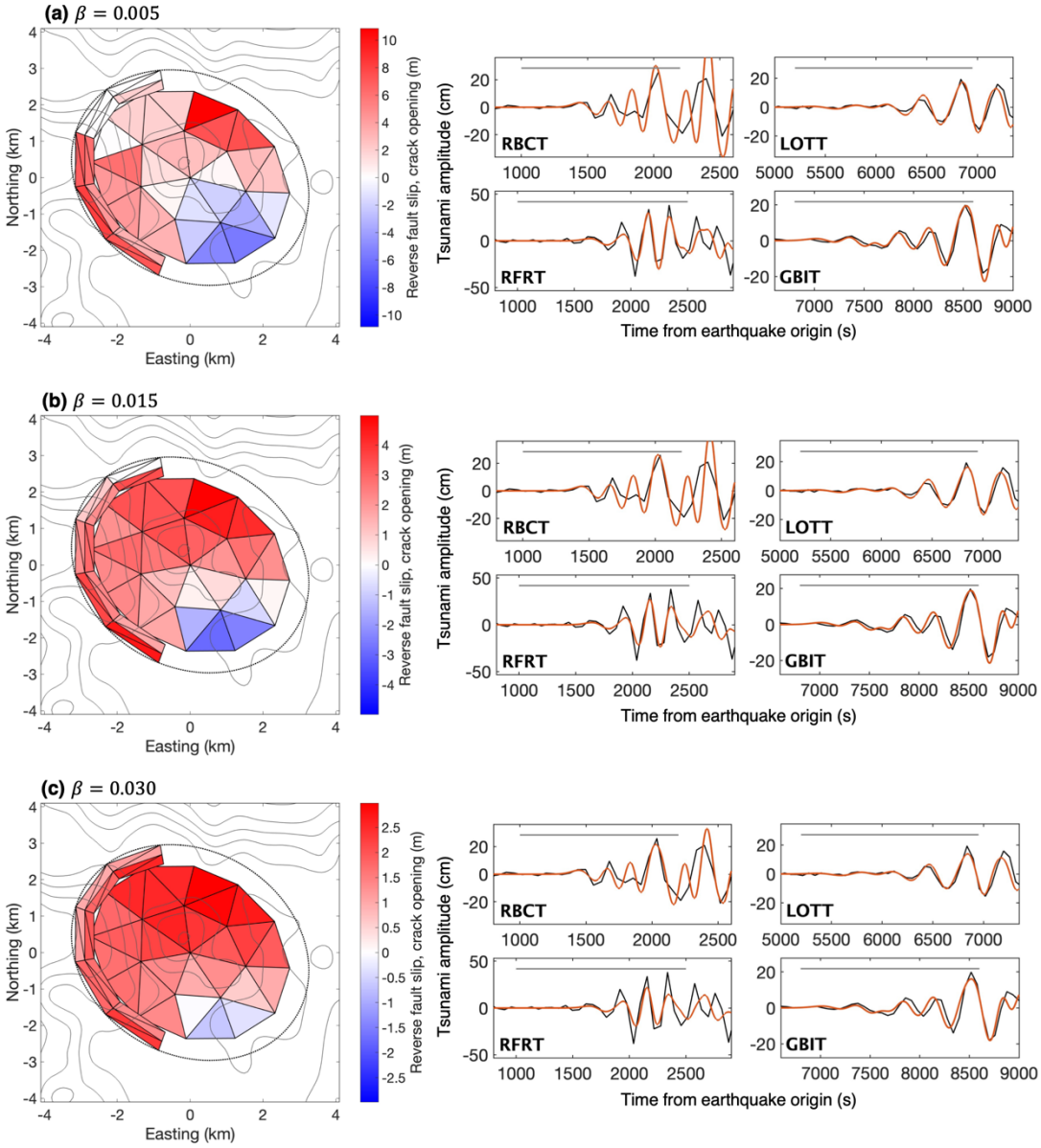

Figure S10. Source models inverted with different damping parameters β of (**a**) 0.005, (**b**) 0.015, and (**c**) 0.030. (Left) Dislocations of the fault-crack source system determined by the tsunami inversion. See captions of Figure 3b in Main Text. (Right) Synthetic tsunami waveforms from the models (red), compared with observed waveforms (black). See the caption of Figure 4b in Main Text. By taking the balance between the solution smoothness and the tsunami waveform fit, we use β of 0.015.

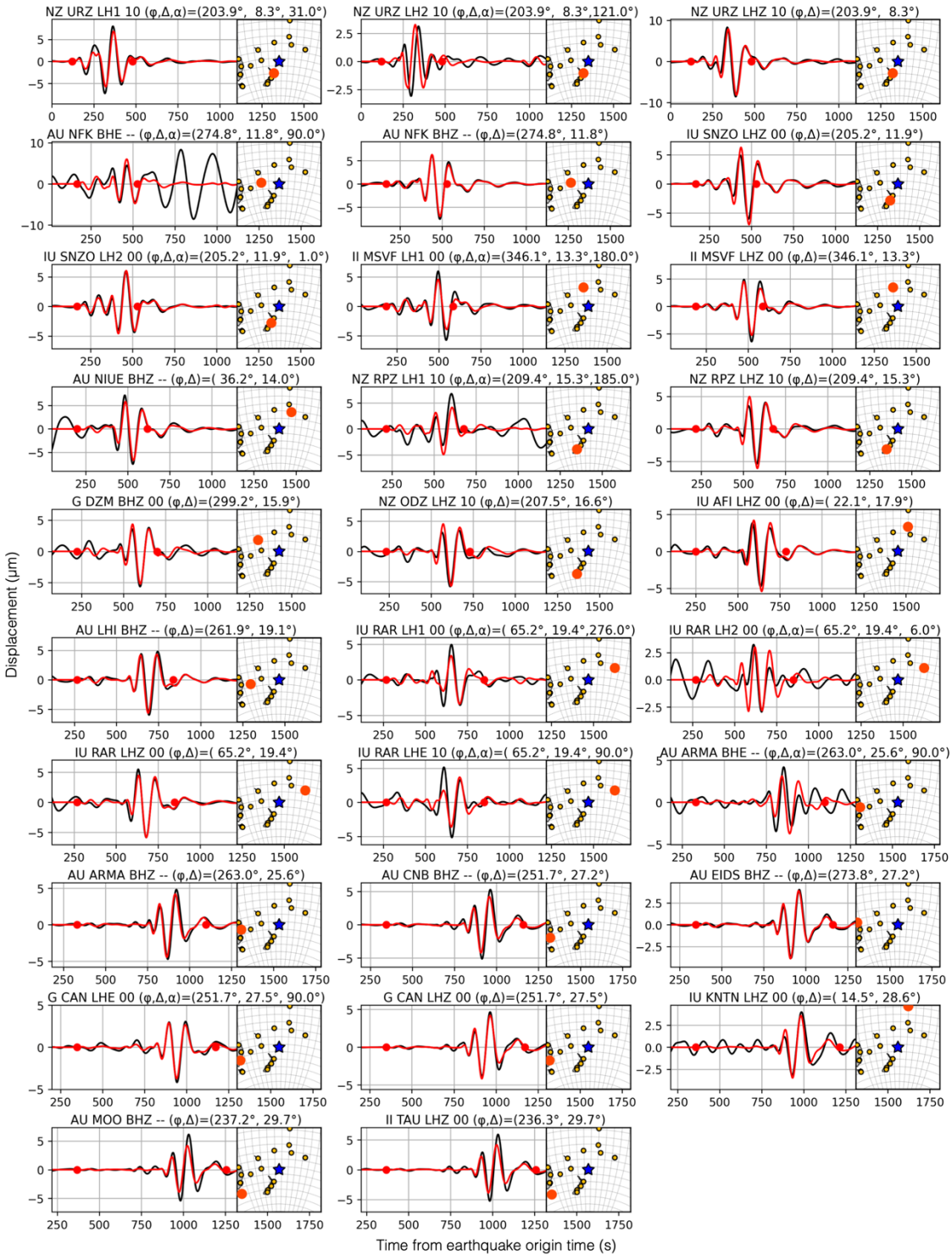

Figure S11. Model performance of the MT analysis for the 2009 earthquake. Red and black lines represent synthetic and observed waveforms, respectively. The time window for the inversion is indicated by red dots.

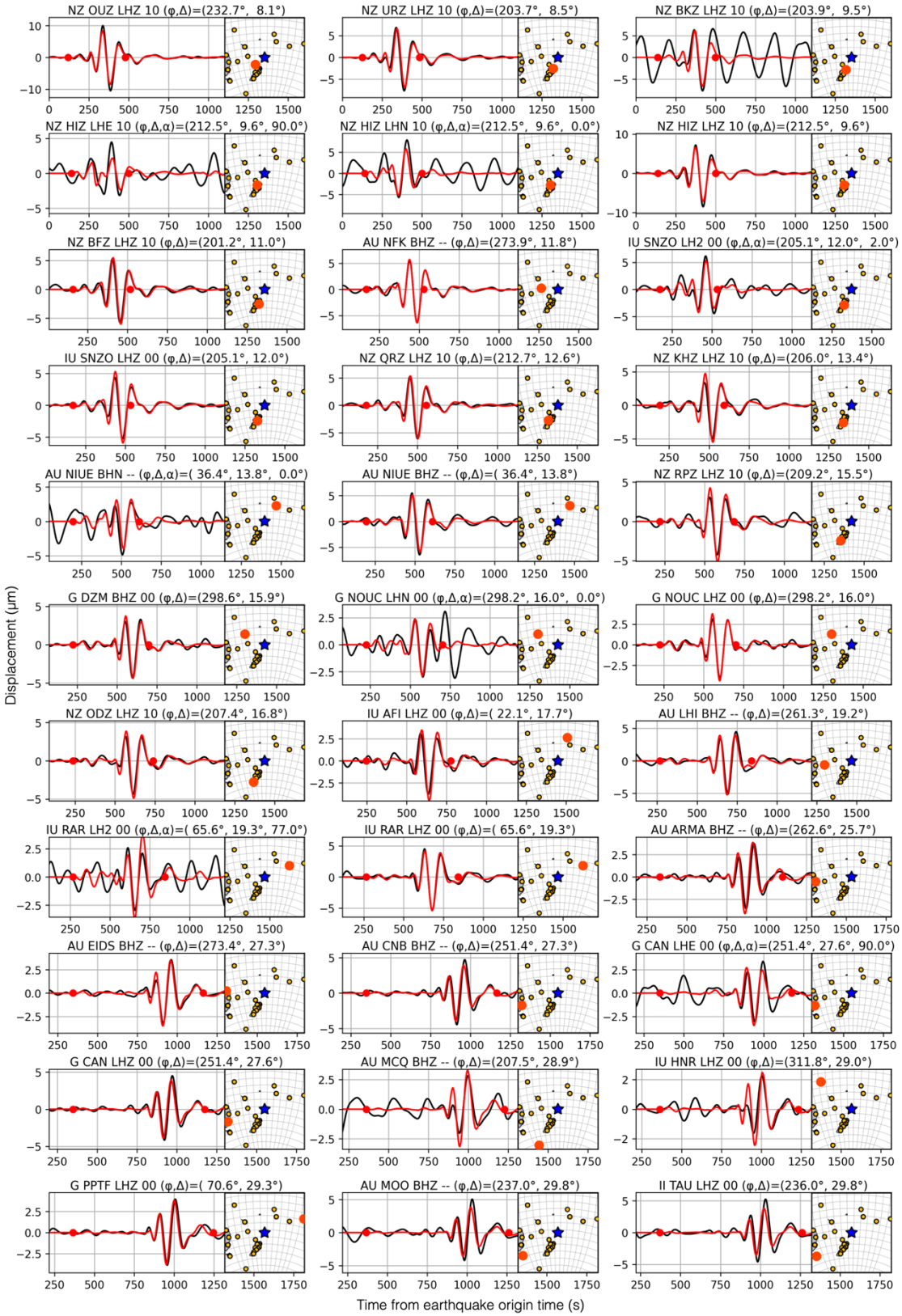

Figure S12. Same as Figure S11, but for the 2017 earthquake.

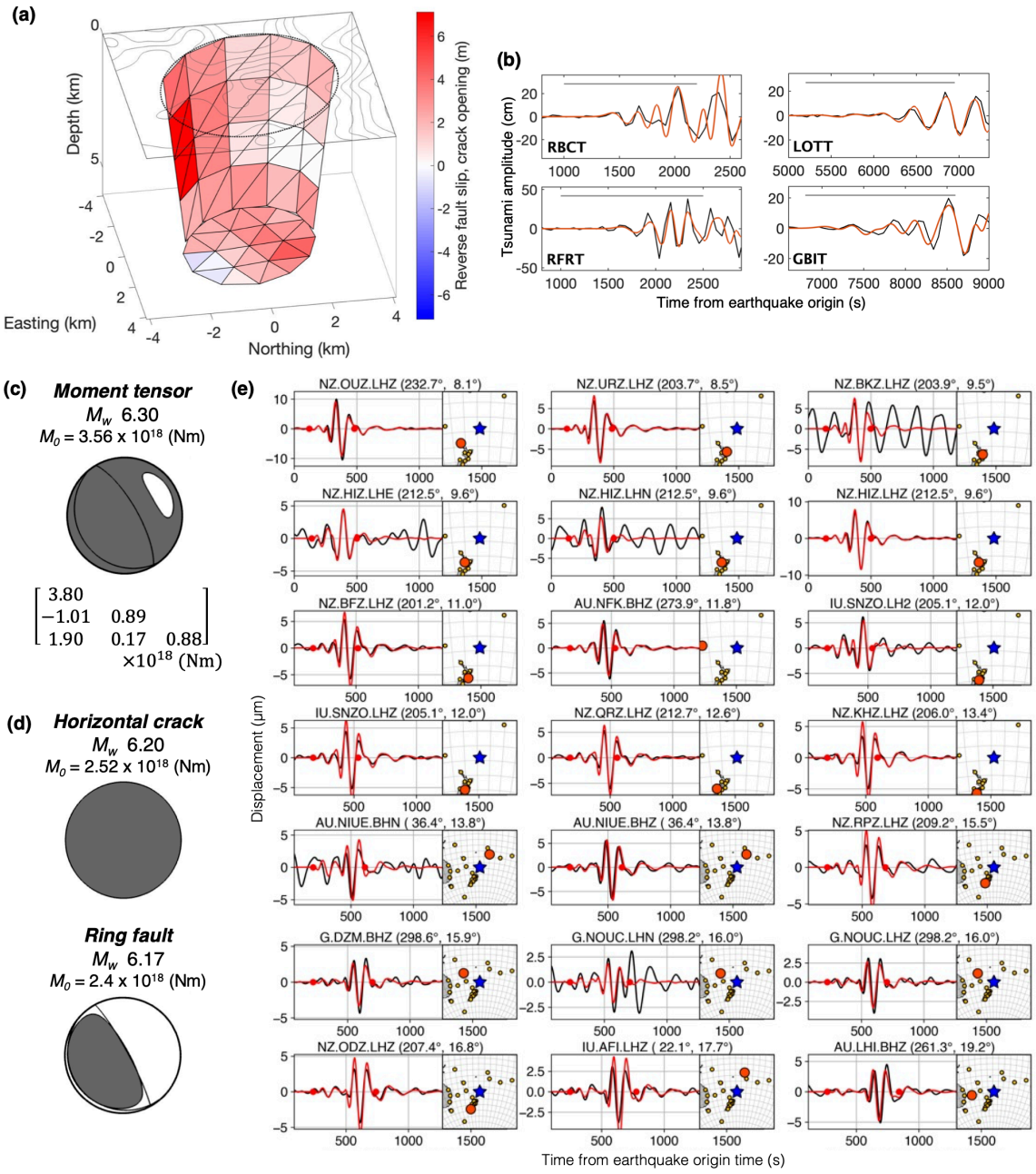

Figure S13. Fault-crack composite source model with a horizontal crack at a depth of 6 km in the crust. (**a**) Dislocations of the fault-crack source system determined by the tsunami waveform inversion. See the caption of Figure 3b in Main Text. (**b**) Synthetic tsunami waveforms from this model (red), compared with observed waveforms (black). See the caption of Figure 4b in Main Text. (**c**–**e**) Results of long-period seismic waveform modeling. See the caption of Figure 4c–e in Main Text.

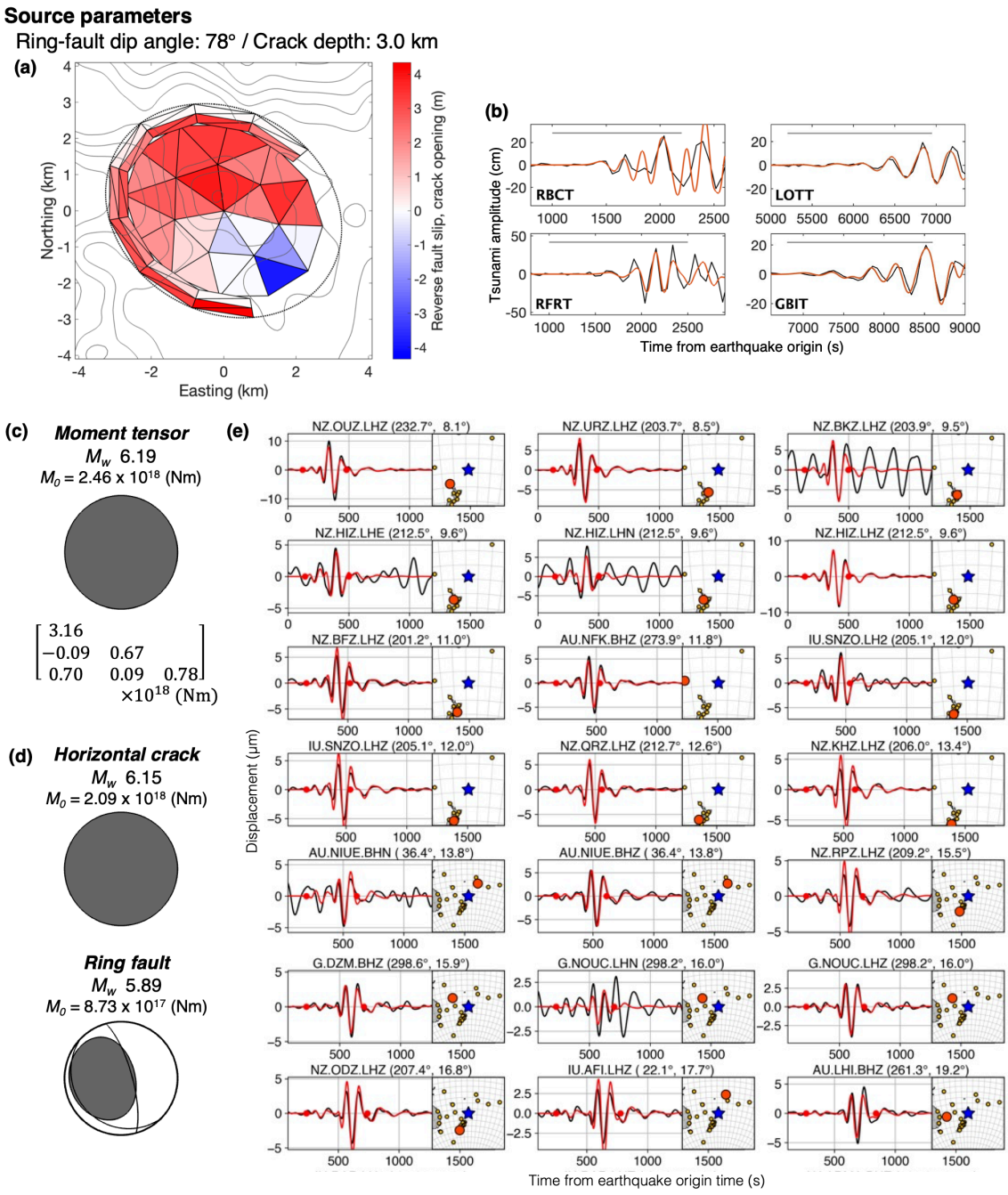

Figure S14. Same as Figure S13, but for a fault-crack composite source model with a longer ring fault with a central angle of 240°.

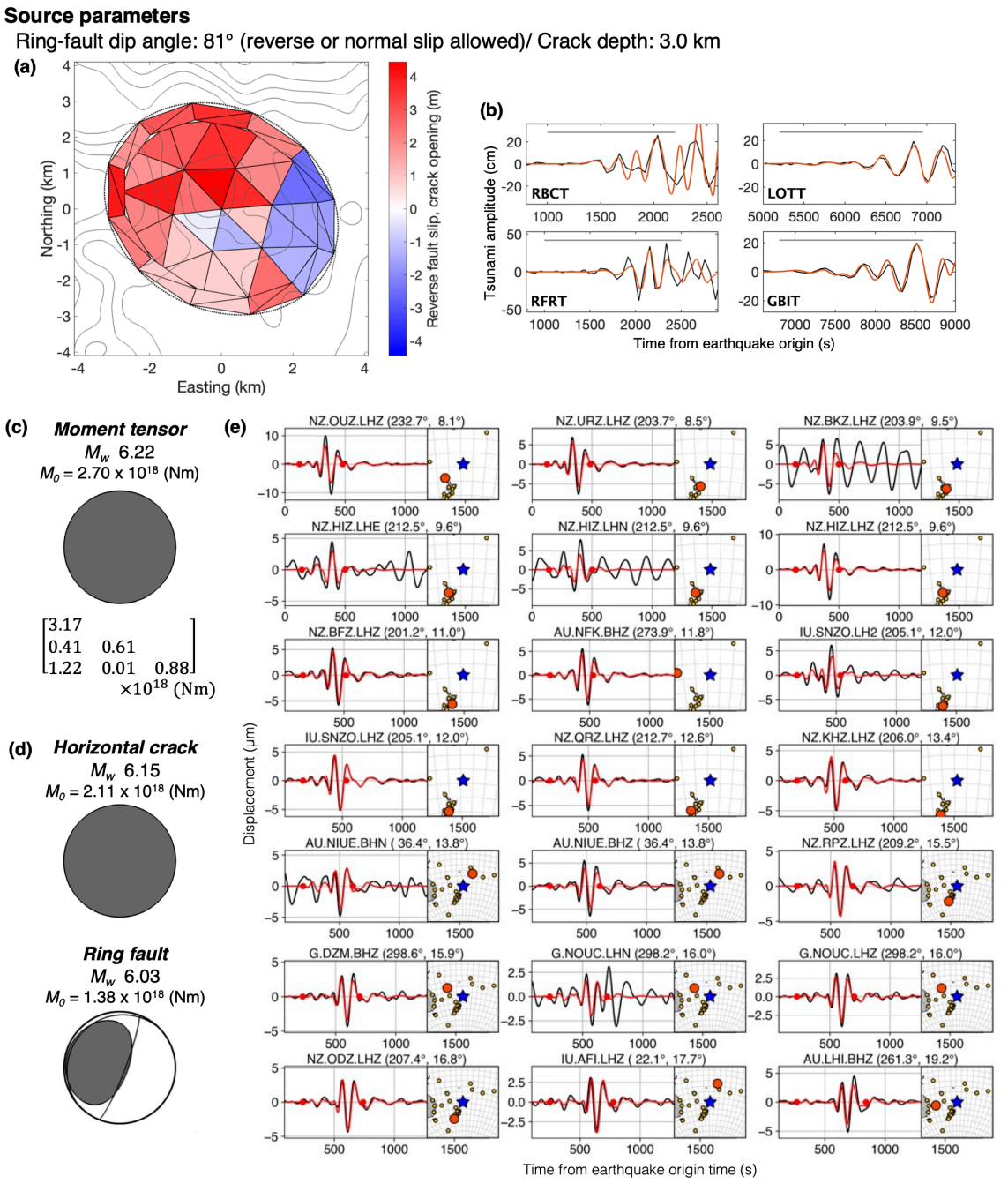

Figure S15. Same as Figure S13, but for a fault-crack composite source model with a fully elliptic ring fault, on which reverse or normal slips are allowed.

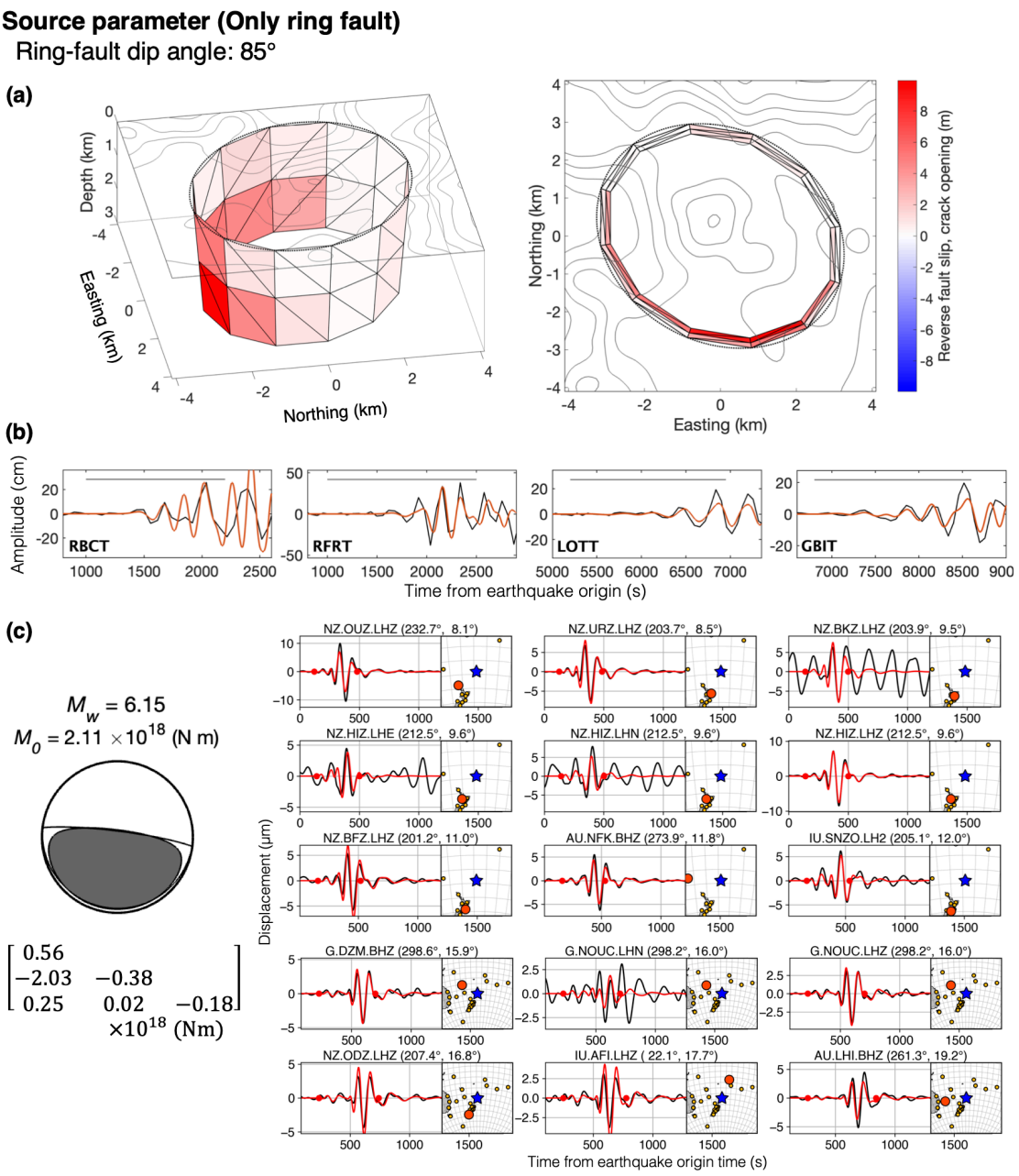

Figure S16. Results of the source modeling for only a fully elliptic ring fault. (**a**) Dislocations of the ring fault determined by the tsunami waveform inversion. (**b**) Synthetic tsunami waveforms from this model (red), compared with observed waveforms (black). (**c**) Results of long-period seismic waveform modeling. (Left) moment tensor of the model, and (right) comparison between synthetic and observed seismic waveforms at representative stations.

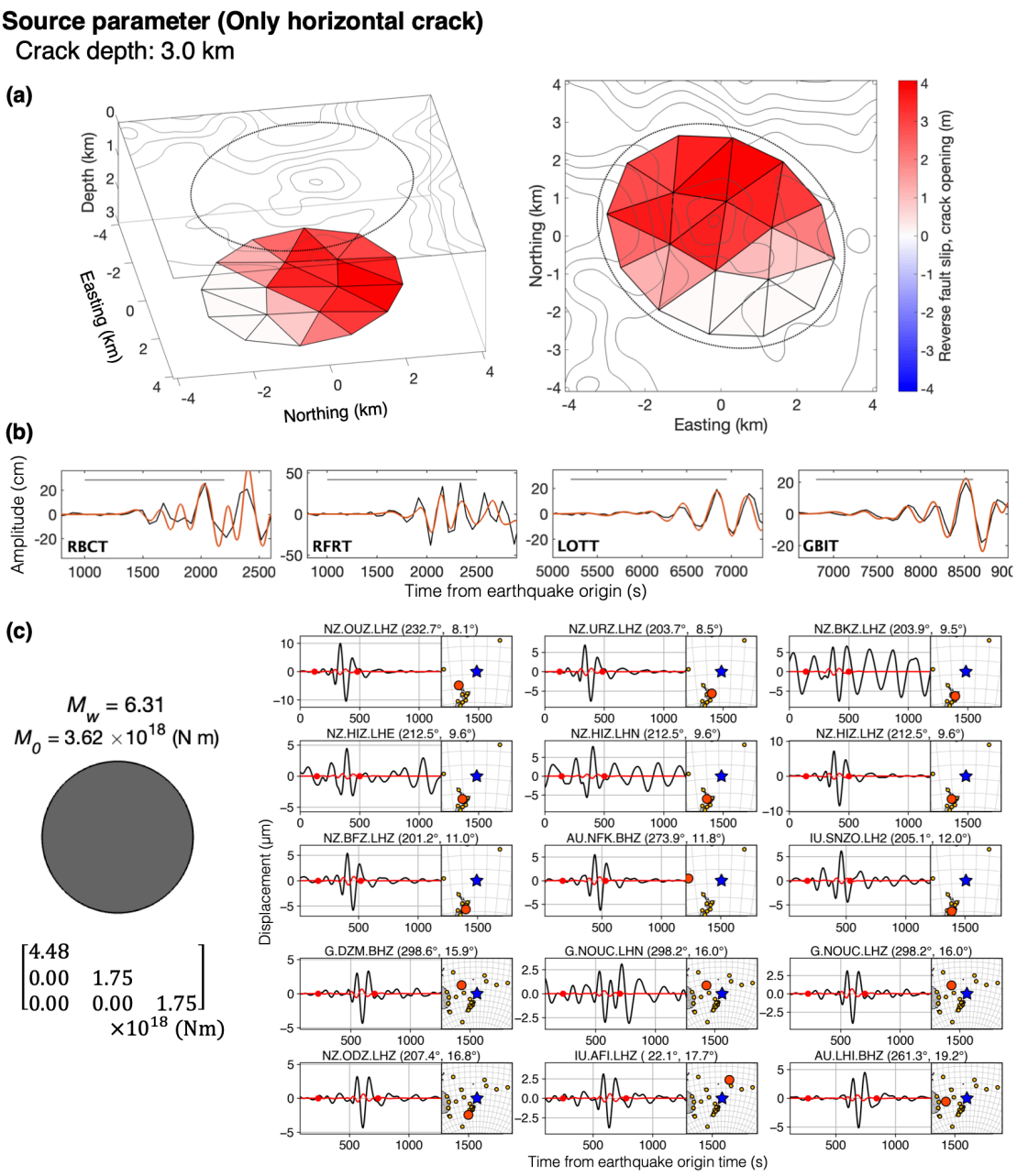

Figure S17. Same as Figure S16, but for only a horizontal crack. In (**a**), dislocations of the horizontal crack determined by the tsunami waveform inversion are shown.

Date	Time	Longitude	Latitude	Depth	M_w	M_s
17 Feb. 2009	03:30:58.6	178.54°W	30.56°S	12.1 km	5.8	6.0
8 Dec. 2017	02:10:03.0	178.56°W	30.49°S	13.4 km	5.8	6.2

Table S1. Earthquake information reported in the GCMT catalogue. Note that the depth may be determined at a greater depth than the accurate depth to maintain the stability of solutions (Ekström et al., 2012).

Moment tensor	M_w	M_0 (10^{18} N m)	Moment tensor (10^{18} N m)					
			M_{rr}	$M_{\theta\theta}$	$M_{\varphi\varphi}$	$M_{r\theta}$	$M_{r\varphi}$	$M_{\theta\varphi}$
Composite, $\boldsymbol{M}$	6.24	2.87	3.59	0.95	0.85	-0.18	0.98	0.07
Horizontal crack, $\boldsymbol{M}_{HC}$	6.19	2.44	3.02	1.18	1.18	0.00	0.00	0.00
Ring-fault, $\boldsymbol{M}_{RF}$	5.96	1.11	0.57	-0.23	-0.34	-0.18	0.98	0.07

Table S2. Moment tensors of our best-fit source model (Figure 3b in Main Text) of the 2017 earthquake: the moment tensor of the model $\boldsymbol{M}$ (= $\boldsymbol{M_{HC}}$ + $\boldsymbol{M_{RF}}$), and the partial moment tensors of the horizontal crack $\boldsymbol{M_{HC}}$ and the ring fault $\boldsymbol{M_{RF}}$.

Event	M_w	M_0 (10^{18} N m)	Moment tensor (10^{18} N m)						$t_c = t_h$ (s)
			M_{rr}	$M_{\theta\theta}$	$M_{\varphi\varphi}$	$M_{r\theta}$	$M_{r\varphi}$	$M_{\theta\varphi}$	
2009	6.45	5.92	0.615	-0.276	-0.339	-2.201	-5.468	0.103	4.0
2017	6.45	5.98	0.505	-0.186	-0.320	-2.441	-5.437	0.134	3.0

Table S3. Deviatoric moment tensor inversion results for the 2009 and 2017 earthquakes using long-period seismic data. We assume that the centroid time shift t_c and the half duration t_h are the same. Note that two elements representing the vertical dip-slip ($M_{r\theta}$ and $M_{r\varphi}$) are poorly determined because of their weak excitation of long-period seismic waves (Kanamori & Given, 1981; Sandanbata, Kanamori, et al., 2021).

Data Set S1. Fault-crack composite source model (separate file). This dataset includes four models presented in Figure 3b in Main Text.

References

Aki, K., & Richards, P. G. (1980). *Quantitative seismology: theory and methods* (Vol. 842). Freeman San Francisco, CA.

Baba, T., Takahashi, N., Kaneda, Y., Ando, K., Matsuoka, D., & Kato, T. (2015). Parallel Implementation of Dispersive Tsunami Wave Modeling with a Nesting Algorithm for the 2011 Tohoku Tsunami. *Pure and Applied Geophysics*, *172*(12), 3455–3472. https://doi.org/10.1007/s00024-015-1049-2

Dahlen, F. A., & Tromp, J. (1998). *Theoretical Global Seismology*. Princeton University Press. https://doi.org/10.1515/9780691216157

Duputel, Z., Rivera, L., Kanamori, H., & Hayes, G. (2012). W phase source inversion for moderate to large earthquakes (1990–2010). *Geophysical Journal International*, *189*(2), 1125–1147. https://doi.org/10.1111/j.1365-246X.2012.05419.x

Dziewonski, A. M., & Anderson, D. L. (1981). Preliminary reference Earth model. *Physics of the Earth and Planetary Interiors*, *25*(4), 297–356. https://doi.org/10.1016/0031-9201(81)90046-7

Ekström, G., Nettles, M., & Dziewoński, A. M. (2012). The global CMT project 2004–2010: Centroid-moment tensors for 13,017 earthquakes. *Physics of the Earth and Planetary Interiors*, *200-201*, 1–9. https://doi.org/10.1016/j.pepi.2012.04.002

Fukao, Y., Sandanbata, O., Sugioka, H., Ito, A., Shiobara, H., Watada, S., & Satake, K. (2018). Mechanism of the 2015 volcanic tsunami earthquake near Torishima, Japan. *Science Advances*, *4*(4), eaao0219. https://doi.org/10.1126/sciadv.aao0219

Gusman, A. R., Kaneko, Y., Power, W., & Burbidge, D. (2020). Source process for two enigmatic repeating vertical‐T CLVD tsunami earthquakes in the kermadec ridge. *Geophysical Research Letters*, *47*(16). https://doi.org/10.1029/2020gl087805

Hanks, T. C., & Kanamori, H. (1979). A moment magnitude scale. *Journal of Geophysical Research*, *84*(B5), 2348. https://doi.org/10.1029/jb084ib05p02348

Hayes, G. P., Rivera, L., & Kanamori, H. (2009). Source Inversion of the W-Phase: Real-time Implementation and Extension to Low Magnitudes. *Seismological Research Letters*, *80*(5), 817–822. https://doi.org/10.1785/gssrl.80.5.817

Ho, T.-C., Satake, K., & Watada, S. (2017). Improved phase corrections for transoceanic tsunami data in spatial and temporal source estimation: Application to the 2011 Tohoku earthquake. *Journal of Geophysical Research, [Solid Earth]*, *122*(12), 10155–10175. https://doi.org/10.1002/2017jb015070

Kajiura, K. (1963). The Leading Wave of a Tsunami. *Bulletin of the Earthquake Research Institute, University of Tokyo*, *41*(3), 535–571. Retrieved from https://ci.nii.ac.jp/naid/120000866529/

Kanamori, H. (1977). The energy release in great earthquakes. *Journal of Geophysical Research*, *82*(20), 2981–2987. https://doi.org/10.1029/jb082i020p02981

Kanamori, H., & Given, J. W. (1981). Use of long-period surface waves for rapid determination of earthquake-source parameters. *Physics of the Earth and Planetary Interiors*, *27*(1), 8–31. https://doi.org/10.1016/0031-9201(81)90083-2

Kanamori, H., & Rivera, L. (2008). Source inversion of Wphase: speeding up seismic tsunami warning. *Geophysical Journal International*, *175*(1), 222–238. https://doi.org/10.1111/j.1365-246X.2008.03887.x

Kawakatsu, H. (1996). Observability of the isotropic component of a moment tensor. *Geophysical Journal International*, *126*(2), 525–544. https://doi.org/10.1111/j.1365-246X.1996.tb05308.x

Kawakatsu, H., & Yamamoto, M. (2015). 4.15 - Volcano Seismology. In G. Schubert (Ed.), *Treatise on Geophysics (Second Edition)* (pp. 389–419). Oxford: Elsevier. https://doi.org/10.1016/B978-0-444-53802-4.00081-6

Nikkhoo, M., & Walter, T. R. (2015). Triangular dislocation: an analytical, artefact-free solution. *Geophysical Journal International*, *201*(2), 1119–1141. https://doi.org/10.1093/gji/ggv035

Peregrine, D. H. (1972). Equations for Water Waves and the Approximation behind Them. In R. E. Meyer (Ed.), *Waves on Beaches and Resulting Sediment Transport* (pp. 95–121). Academic Press. https://doi.org/10.1016/B978-0-12-493250-0.50007-2

Persson, P.-O., & Strang, G. (2004). A Simple Mesh Generator in MATLAB. *SIAM Review. Society for Industrial and Applied Mathematics*, *46*(2), 329–345. https://doi.org/10.1137/s0036144503429121

Sandanbata, O., Kanamori, H., Rivera, L., Zhan, Z., Watada, S., & Satake, K. (2021). Moment tensors of ring-faulting at active volcanoes: Insights into vertical-CLVD earthquakes at the Sierra Negra caldera, Galápagos islands. *Journal of Geophysical Research, [Solid Earth]*, *126*(6), e2021JB021693. https://doi.org/10.1029/2021jb021693

Sandanbata, O., Watada, S., Ho, T.-C., & Satake, K. (2021). Phase delay of short-period tsunamis in the density-stratified compressible ocean over the elastic Earth. *Geophysical Journal International*, *226*(3), 1975–1985. https://doi.org/10.1093/gji/ggab192

Sandanbata, O., Watada, S., Satake, K., Kanamori, H., Rivera, L., & Zhan, Z. (2022, February 14). *Sub-decadal Volcanic Tsunamis Due to Submarine Trapdoor Faulting at Sumisu Caldera in the Izu-Bonin Arc. Earth and Space Science Open Archive*. https://doi.org/10.1002/essoar.10510526.3

Shuler, A., Ekström, G., & Nettles, M. (2013). Physical mechanisms for vertical-CLVD earthquakes at active volcanoes. *Journal of Geophysical Research, [Solid Earth]*, *118*(4), 1569–1586. https://doi.org/10.1002/jgrb.50131

Silver, P. G., & Jordan, T. H. (1982). Optimal estimation of scalar seismic moment. *Geophysical Journal International*, *70*(3), 755–787. https://doi.org/10.1111/j.1365-246X.1982.tb05982.x

Takeuchi, H., & Saito, M. (1972). Seismic surface waves. *Methods in Computational Physics*, *11*, 217–295.

Watada, S., Kusumoto, S., & Satake, K. (2014). Traveltime delay and initial phase reversal of distant tsunamis coupled with the self-gravitating elastic Earth. *Journal of Geophysical Research, [Solid Earth]*, *119*(5), 4287–4310. https://doi.org/10.1002/2013jb010841

Weatherall, P., Marks, K. M., & Jakobsson, M. (2015). A new digital bathymetric model of the world's oceans. *Earth and Space*. https://doi.org/10.1002/2015EA000107